RSC Advances

REVIEW

View Article Online
View Journal | View Issue

Cite this: *RSC Adv.*, 2025, **15**, 26104

Advancement of bottom-up precipitation synthesis and applications of barium sulphate nanoparticles

Megawati Zunita, * Dendy Adityawarman, Eveline Iskandar and Rahadian Rizky Ramadhan

Barium sulphate nanoparticles ($BaSO_4$ NPs) have garnered considerable attention owing to their distinctive physicochemical characteristics and varied uses in the polymer industry and medicine. Their synthesis by the bottom-up precipitation process is significantly affected by capping agents, which are crucial for regulating shape and size. $BaSO_4$ nanoparticles exhibit significant potential in medical imaging, reinforcing of bone cement, and administration of cancer therapeutics, while simultaneously improving the tensile strength, thermal stability, and impact resistance of polymers. This review paper examines the influence of diverse capping agents, including polymers, surfactants, and organic compounds, on the shape and size modulation of nanoparticles. It also analyses reactor modifications, such as rotating packed beds, T-mixers, membrane reactors, and spinning disc reactors, to enhance size distribution. This review also emphasises the prospective applications of $BaSO_4$ nanoparticles in medical imaging, targeted medication administration, energy storage, and composite materials. Green synthesis techniques and ionic liquid-assisted methods are examined to enhance the sustainable manufacture of $BaSO_4$ nanoparticles.

Received 13th April 2025
Accepted 2nd July 2025

DOI: 10.1039/d5ra02597d

rsc.li/rsc-advances

1. Introduction

Recently, nanotechnology has undergone many developments in its implementation in various industrial sectors. In general, nanotechnology can be defined as an applied science specifically implemented to manipulate materials on a nanometer scale.[1] The main objective of nanotechnology is to design, enhance, and employ structures at nanometer scale to develop novel materials or improve the efficiency of currently available technologies.[2,3] The development of nanotechnology is mainly related to the synthesis and modification of nanomaterials. Nanomaterials can be composed of metals, ceramics, or in polymer composites.[4–6] The petite size of nanomaterials causes significant changes from the base materials physical, chemical, and mechanical properties.[7,8] These distinctive properties of nanomaterials are leveraged to create more sophisticated technologies. In addition, to the extensively researched carbon nanotubes and fullerenes, the domain of nanomaterials includes a wide variety of forms and compositions, each displaying distinct properties and functionalities. Nanomaterials, with dimensions within the nanoscale range (1–100 nm), exhibit unique properties due to their enhanced surface area to volume ratio and quantum mechanical effects. These properties are attributed to the increased ratio of surface atoms to inside atoms. Nanoparticles, nanowires, and nanotubes are examples of materials with desirable properties at the nanoscale. Nanomaterials can be categorized based on dimensionality, chemistry, and shape. One-dimensional nanomaterials, such as thin films and surface coatings, are used for surface modification and protection. Two-dimensional nanomaterials, like nanowires and nanorods, are used in electronic devices and sensors. Zero-dimensional nanomaterials, like quantum dots and colloidal nanoparticles, are used in drug distribution, bioimaging, and catalysis.

Barium sulfate nanoparticles are one of the metal-based nanomaterials that has been widely explored and developed, proven by the increment of number of studies on barium sulphate nanoparticles every year. The graph in Fig. 1 sums up the quantity of studies conducted to examine barium sulphate nanoparticles.

Barium sulfate is an unique material due to its physicochemical properties, such as relatively high specific gravity (4.5), opaqueness to X-rays, and inertness.[9,10] Barium sulfate nanoparticles have up-and-coming development prospects in various technological applications. Barium sulphate can be used as an important filler material in the plastics, rubber, printing inks, and paint industries.[11–14] To gain more benefit from this material, barium sulfate has been developed as a nanomaterial through various physical and chemical methods. Barium sulfate nanoparticles have highly promising prospects for development in various technological applications, including as an inert contrast agent and shielding material in advanced

Chemical Engineering Department, Faculty of Industrial Technology, Institut Teknologi Bandung, Jalan Ganesha 10, Bandung, West Java, 40132, Indonesia. E-mail: m.zunita@itb.ac.id

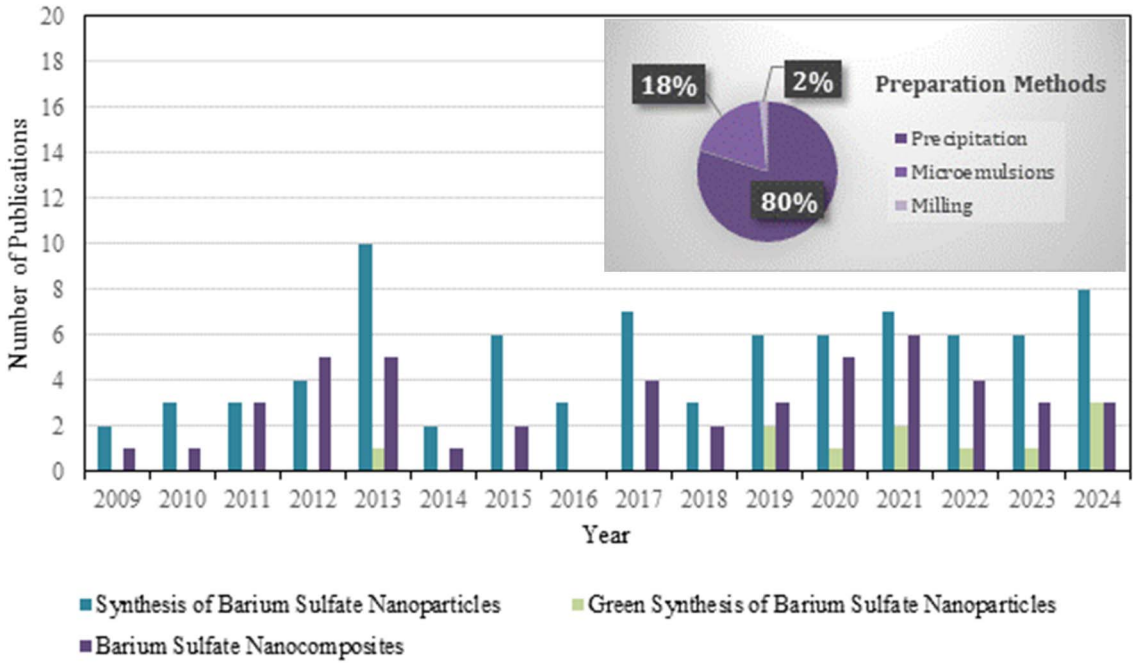

Fig. 1 Number of publications related to barium sulfate nanoparticles bottom-up synthesis and barium sulfate nanoparticles applications indexed by Scopus, Queries (TITLE-ABS-KEY ("synthesis of barium sulfate nanoparticles"), TITLE-ABS-KEY ("green synthesis of barium sulfate nanoparticles"), and TITLE-ABS-KEY ("barium sulfate nanocomposites")); accessed on: August 21st, 2024.

medical imaging technology and targeted alpha-therapy, battery efficiency improvement, energy storage systems, and composite material additives.[15–20] This applications is achievable because barium sulfate nanoparticles tend to have a large surface area with diverse morphology depending on its production method.[21–23]

Generally, nanoparticle synthesis can be divided into top-down and bottom-up route.[24,25] As shown in Fig. 2, bottom-up approach entails building larger nanostructures from smaller atoms and molecules whereas the top-down approach involves scaling down materials to the nanoscale.[26] Top-down synthesis route typically using physical method to obtain nanosize particles from bulk materials, such as ball milling and laser ablation.[27,28] These top-down methods have high production batch capacity and usually no need to chemically purify the products. However, it requires more sophisticated technology and consumes a lot of electricity. In contrast, bottom-up approach to nanoparticle synthesis is favored for creating nanoscale materials due to its ability to yield more uniform sizes, shapes, and distributions compared to the products of top-down synthesis methods.[29]

The bottom-up synthesis of barium sulphate nanoparticles is mainly classified to two methods: microemulsions and precipitation. The microemulsions method involves the synthesis of nanoparticles within nanodroplets of a water-in-oil (w/o) microemulsion system consists of water, oil (typically cyclohexane), and surfactants. The method utilizes the unique properties of microemulsions as nanoreactors where two reactants, *i.e.* $BaCl_2$ and K_2SO_4 would be mixed at the droplet interfaces, leading to the precipitation of nanoparticles.[30] As

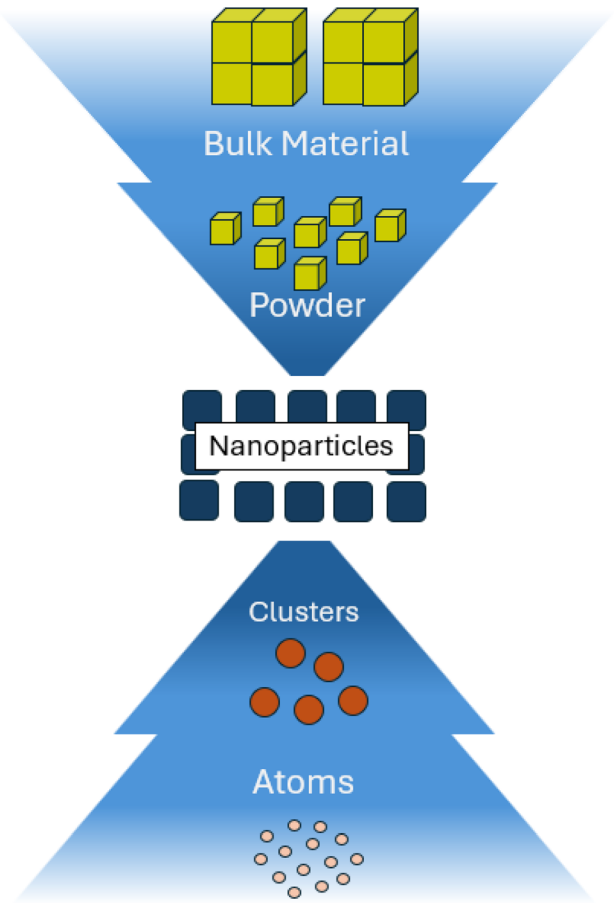

Fig. 2 Illustration of top-down and bottom-up approaches of nanoparticles synthesis.

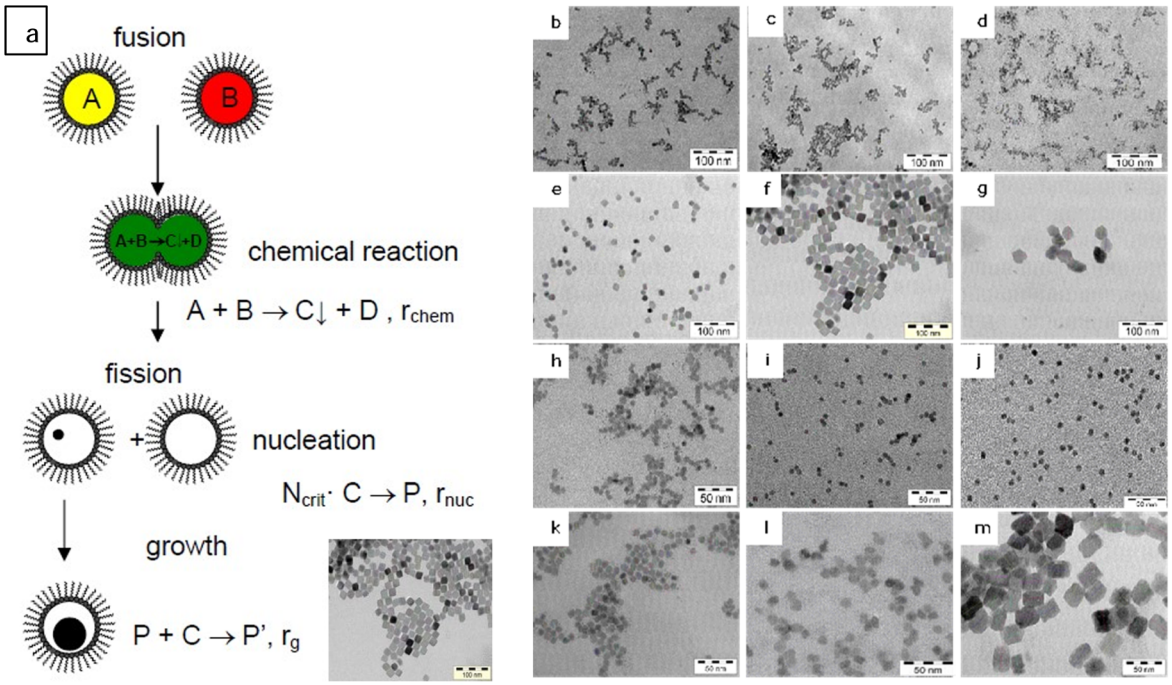

Fig. 3 (a) Scheme of $BaSO_4$ nanoparticles production process using microemulsions system; TEM of $BaSO_4$ nanoparticles with various microemulsions concentration: set 1 with $K_2SO_4 = 0.1$ mol L^{-1} and $BaCl_2$ = (b) 0.1 mol L^{-1}, (c) 0.075 mol L^{-1}, (d) 0.05 mol L^{-1}, (e) 0.025 mol L^{-1}, (f) 0.01 mol L^{-1}, (g) 0.005 mol L^{-1}; set 2 with $BaCl_2 = 0.1$ mol L^{-1} and K_2SO_4 = (h) 0.1 mol L^{-1}, (i) 0.075 mol L^{-1}, (j) 0.05 mol L^{-1}, (k) 0.025 mol L^{-1}, (l) 0.01 mol L^{-1}, (m) 0.005 mol L^{-1} (reproduced from ref. 30 with permission from Otto-von-Guericke Universität Magdeburg, copyright 2007).

illustrated in Fig. 3a, the production of barium sulfate nanoparticles in a semi-batch stirred reactor involves two microemulsions: a stock microemulsion containing encapsulated K_2SO_4 and a feed microemulsion containing $BaCl_2$. The interaction between these microemulsions leads to droplet fusion, which serves as the chemical reaction step for the formation of liquid $BaSO_4$. When the number of molecules reaches a critical threshold (N_{crit}) necessary for stability through nucleation in the fission step, the particle growth rate is controlled by the consumption of liquid $BaSO_4$ molecules (C).

This method has several benefits, including refined size and distribution control due to droplet fusion and fission reaction in surfactant's protective monolayer, high interfacial area, and efficient tuning by adjusting surfactant concentration, stirring rates, and reactant ratios.[31] Based on the observation of the TEM results of $BaSO_4$ nanoparticles gained from various concentration ratio in Fig. 3b–m, the decrement of K_2SO_4 or increment of $BaCl_2$ would affect the primary chemical reaction stoichiometry condition and the particles' morphology. If the reaction occurs at relatively balanced stoichiometric feed ratio, the particle size of $BaSO_4$ would be smaller (6 nm). Conversely, $BaSO_4$ particles formed under a non-stoichiometric reaction system would have larger mean diameter (up to 31 nm) due to lower supersaturation condition. This deviation in stoichiometric feed ratio would alter the shape of obtained $BaSO_4$ nanoparticles from spherical to cubical structure. Hence, this method has more precise parameters for tuning particle size and shape. However, microemulsions method of nanoparticles synthesis also has some drawbacks, such as complexity of phase behavior, dependency on the stability of surfactant systems, narrow operating condition windows, and limitation of size tuning in highly-viscous mixture systems that may affect the product's quality in large-scale synthesis. On the other hand, the precipitation method has been widely used for bottom-up synthesis of barium sulfate nanoparticles with high purity.[32] This method involves the direct mixing of barium and sulfate solutions under constant stirring to yield $BaSO_4$, which has low solubility in water, as represented by the following reaction:

$$Ba^{2+}(aq) + SO_4^{2-}(aq) \rightarrow BaSO_4(s)$$

Similar to the microemulsion method, several key parameters can be adjusted to prevent excessive growth or agglomeration of nanoparticles, such as concentration ratio, temperature, mixing rate, and pH. Therefore, the precipitation method is preferred for its simplicity and economic feasibility compared to other approaches.[33,34] This method is also relatively more flexible to be established on a commercial scale for continuous production.[35,36] Hence, the precipitation method is more commonly utilized in research on barium sulfate nanoparticles compared to other methods. This statement is supported by the data of the number of publications regarding to various nanoparticle synthesis methods, as presented in the subset of Fig. 1.

Nanoparticles precipitation usually requires a capping agent with specific functional group to prevent overgrowth and agglomeration of nanoparticles.[37] Some of these experiments implies that synthesis using different capping agents leads to alteration of nanoparticle structures.[38–40] Capping agent also

influence the dispersion characteristics of barium sulfate nanoparticles in solvents.[41] Some studies revealed that different concentration of capping agent and pH would results in some variety of size and morphology of nanosize final products.[42–45] Nanoparticle synthesis can be conducted by using specific ionic liquid (IL). Ionic liquid developed as an alternative template in the synthesis of barium sulfate nanoparticles to pursuit an environmentally friendly approach.[46]

Nanoparticles synthesis with the precipitation method can be carried out in various types of reactors. Several types of reactors have been widely developed and modified for barium sulfate nanoparticle precipitation, including capillary microreactor, membrane reactor, spinning disk reactor, and rotating packed bed (RPB).[32,47–51] The difference in reactor types affects the size of the barium sulfate nanoparticles produced from the precipitation process. This differences occur mainly because of the different types and sizes of reactors affect the homogeneity and diffusion of raw materials during the barium sulfate nanoparticle manufacturing process.[52]

In this paper review, several synthesis using precipitation methods to obtain barium sulfate nanoparticles ($BaSO_4$ NPs) with capping agents have been summarized. We compared and discussed how the influence of variations in capping agents and types of reactors affect the morphology and mean particle diameter of barium sulfate nanoparticles. We also emphasized the advantages and applications of these nanoparticles in various sectors, including enhanced mechanical strength, improved thermal stability, and other beneficial features in the medical and polymer industry. Some green synthesis methods are mentioned in separated chapter of this paper review to enhance the discussion about environmentally friendly barium sulphate nanoparticles synthesis method, which is considered a prominent topic in recent research related to chemical synthesis.

2. Synthesis of $BaSO_4$ nanoparticles with precipitation method

Precipitation is one of the most common methods to synthesize barium sulfate nanoparticles. This synthesis technique has many advantages, such as the simplicity of the mechanism, cost and energy effectiveness, easier to scaled-up, and faster reaction.[53,54] However, precipitation method has several drawbacks, including difficulty to maintain quality control over particle size and distribution and excessive agglomeration due to van der Waals force on the nanoparticles.[55,56] The precipitation method is carried out by dissolving a constituent material in a solvent before added with another feed solution and stirred continuously at certain rate. This action would bring the solution into saturated state as a precursor, leading to nucleation of specific nanoparticles precipitate according to the reactants.[57] The precipitation of nanoparticles usually involves a compound to tune and stabilize the nucleation and growth of the nanoparticles. This compound is known as capping agent. Some capping agents often used in precipitation of barium sulfate nanoparticles are surfactants and various organic polar compounds. These capping agents have the capability to hinder further growth of barium sulfate particles so that their particle size distribution becomes narrower and smaller while also influencing their morphology.[58]

2.1 $BaSO_4$ nanoparticles precipitation involving organic compounds

Several organic compounds have been utilized as precipitating and capping agents in barium sulfate nanoparticle synthesis. Bala *et al.* (2005) reported $BaSO_4$ nanoparticles synthesis in a water–ethanol medium. This experiment was done by

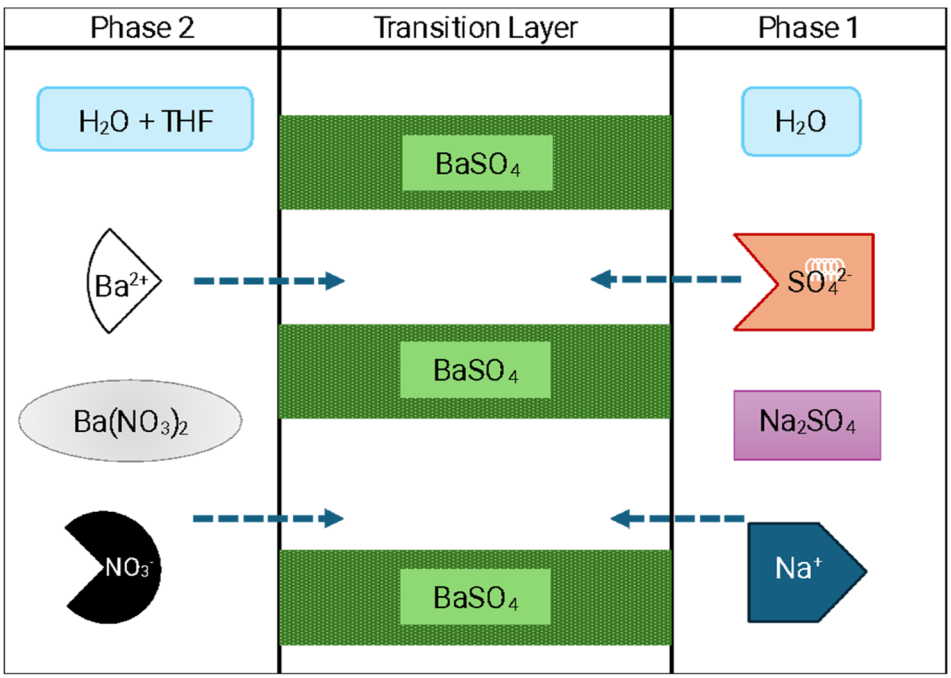

Fig. 4 $BaSO_4$ nanoparticle precipitation scheme in water–THF system.

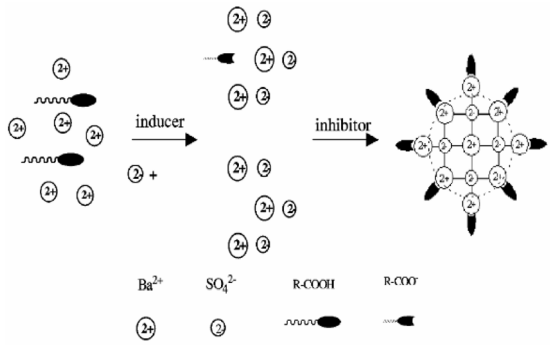

Fig. 5 Scheme of $BaSO_4$ nanoparticles precipitation modified by organic acids (reproduced from ref. 71 with permission from Springer, copyright 2007).

preparing 20 mL of 0.5 M $BaCl_2$ solution and 20 mL of absolute ethanol before adding 10 mL of 1.0 M $(NH_4)_2SO_4$ into the solution.[59] The self-dispersed $BaSO_4$ nanoparticles obtained from this precipitation method have an elliptical shape and a mean particle size of 36 nm, as presented in Fig. 6a. These nanoparticles can disperse with hydrodynamic diameter of 24.3 nm in ethanol suspension and can expand by dispersion in water to 86.5 nm. The morphology of $BaSO_4$ nanoparticles from this study is not completely round as it have some mesopores around 6–8 nm, giving some leverage up to 1.12%-wt of ethanol absorption and consequently rising their ability to disperse in organic solution.[60] The inhibition of $BaSO_4$ crystal growth was due to ethoxide group linkage from ethanol on their surface which forms a protective layer.[61]

A later study conducted by Ramaswamy *et al.* (2011) confirms that compositions of ethanol/water mixed solvents in barium sulfate nanoparticles precipitation would significantly influence the average size of nanoparticles.[62] The result shows declining tendency of $BaSO_4$ nanoparticle size from 85 nm to 54 nm due to increment of ethanol in water–ethanol solvent from 30% to 70%. A more spherical shape of $BaSO_4$ nanopowder is achieved by increasing the ethanol composition in the solvent. The same group also investigated different approaches of $BaSO_4$ nanoparticles precipitation in water-benzene solvent system.[63] This approach was chosen in consideration that benzene is more difficult to dissolve the reactants ($BaCl_2$ and Na_2SO_4 solution) than water, thus the crystallization in this reaction is more reachable.[64] The optimal condition for $BaSO_4$ nanoparticles in this experiment is achieved by addition of 95% benzene in water mixed solvent system

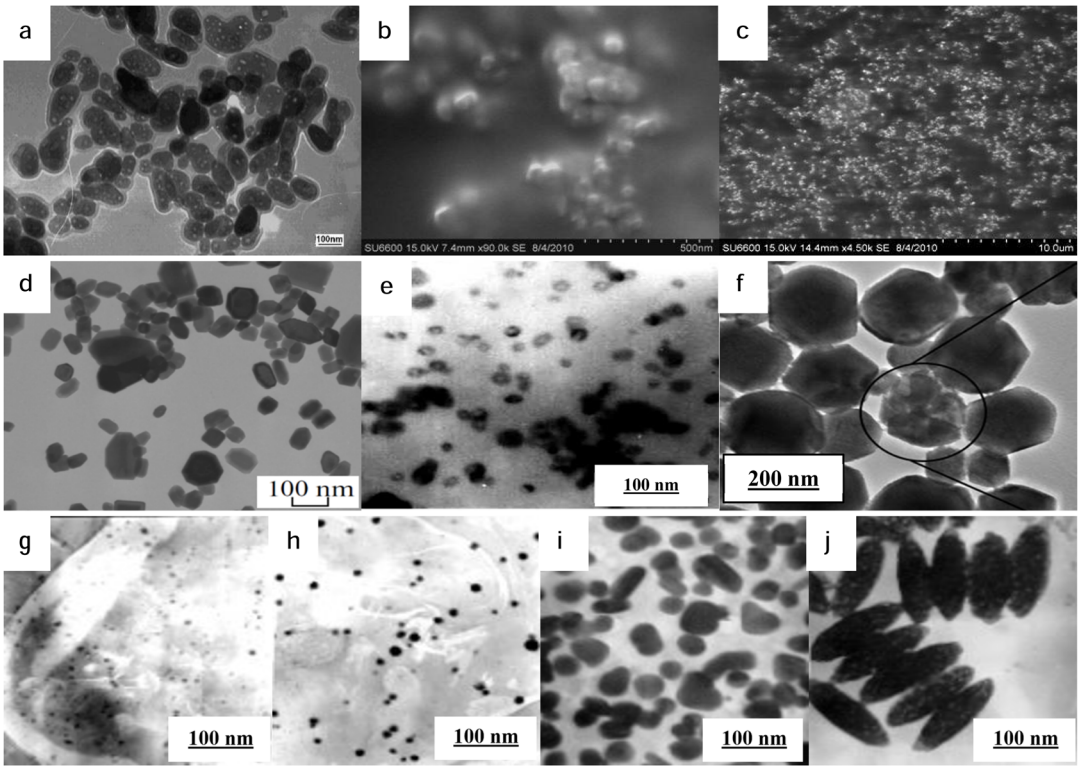

Fig. 6 (a) TEM images of $BaSO_4$ nanoparticles in ethanol–water medium (reproduced from ref. 59 with permission from Elsevier, copyright 2005); (b) and (c) FESEM images of $BaSO_4$ nanoparticles using pure water solvent and 95%-v/v benzene–water mixed solvent, respectively (reproduced from ref. 63 with permission from VBRI Press, copyright 2012); (d) TEM image of $BaSO_4$ particles at phase interface with H_2O : THF ratio of 1 : 1 (reproduced from ref. 65 with permission from Springer, copyright 2015); (e) TEM images of $BaSO_4$ nanoparticles obtained from 3rd approach with addition of 3%-wt stearic acid (reproduced from ref. 71 with permission from Springer, copyright 2007); (f) TEM images of $BaSO_4$ nanoparticles formation in the presence of NTA (reproduced from ref. 74 with permission from the Royal Society of Chemistry, copyright 2006); (g) TEM images of $BaSO_4$ nanoparticles obtained from synthesis with EDTA at pH = 4.5 (13 nm); (h) pH = 6.5 (23 nm); (i) pH = 9.5 (73 nm); (j) pH = 11.5 (89 nm) (reproduced from ref. 43 with permission from Elsevier, copyright 2003).

with an average particle size of 35.995 nm. Although the particle size is still bigger than the nanoparticles obtained from pure water solvent (30.466 nm), 95%-benzene in water solvent system still chosen as the optimal ratio since it has better agglomeration inhibition and homogeneous distribution of the $BaSO_4$ nanoparticles. This statement is supported by visual analysis using FESEM images of $BaSO_4$ nanoparticles produced with addition of pure water solvent and 95%-v/v benzene–water mixed solvent in Fig. 6b and c, respectively.

Meanwhile, Boguslavskii *et al.* (2015) developed an barium sulfate precipitation technique using water–tetrahydrofuran (THF) solvent system.[65] In a nonequilibrium system of water–THF solvent, 0.01 mol per L Na_2SO_4 were introduced to $Ba(NO_3)_2$ to create an interphase transition layer until their final concentration is at 7.7×10^{-2} mol L^{-1} and 4.35×10^{-3} mol L^{-1}, respectively. As illustrated in Fig. 4, the precipitation reaction mechanism involves several key points of nanoparticles dynamics in the transition layer, including the diffusion between solvent and the reactants, leading to the occurrence and dynamic movements of Bernard cells where the nucleation of $BaSO_4$ is bound to happen. In the context of precipitation reaction of $BaSO_4$, Bernard cells refer to molecules that undergo convective motion in a specific vortex-like pattern due to the temperature gradient in a system, instigate alteration of the particles' morphology.[66,67] Interphase transition layer stabilization in this reaction is also affected by intensified mass transfer because of surface tension gradient of the interface layer between two phases, known as Marangoni effect.[68–70] These surface tension gradients would generate a protective property, leading to selective reaction of $BaSO_4$. As shown in Fig. 6d, the optimal molar ratio of H_2O/THF to obtain homogenous $BaSO_4$ nanoparticles (67 nm) with smallest deviation is at 1 : 1.

In order to enhance the inhibiting effect of nanoparticles synthesis additives, Shen *et al.* (2007) developed a barium sulfate nanoparticles modifier by evaluating several organic acids.[71] This $BaSO_4$ modifier is prescribed with three approaches. The first approach was carried out by adding 0.1 M Na_2SO_4 directly to 0.1 M $BaCl_2$ both in ethanol–water solvent system with ethanol/water volume ratio 1 : 1, then inserting a specific amount of stearic acid. As a result, the optimal amount of stearic acid to minimize the $BaSO_4$ nanoparticles' size is obtained at 3%-wt. The second approach is done by tuning the pH of $BaCl_2$ to 8–9 before added by Na_2SO_4 solution dropwise to attained better dispersion while the third approach was carried out by the similar condition to second approach with exception the pH of Na_2SO_4 is also adjusted to the same amount with $BaCl_2$. This adjustment was done to gain smaller $BaSO_4$ nanoparticles by tuning the supply of Ba^{2+} ion in the reaction system. The final result of the 3rd approach reaction can be seen in Fig. 6e.

In this precipitation reaction, organic acids act as an inducer. The addition of sulfate ion in the solution would make the barium ion surplus, thus it is also the main driving force of the precipitation while organic acid induces barium sulfate nanoparticles formation by attracting barium ions through electrostatic forces.[72] These organic acids is also remarkably inhibit the nanoparticles' growth due to steric hindrance. When the pH adjustment was done by adding ammonia to the solution, organic acids would emit their $RCOO^-$ linkage which then absorbed on the surface to prevent agglomeration of $BaSO_4$ nanoparticles. The overall optimal reaction scheme in third approach as illustrated in Fig. 5 can be described as follows:

$$SO_4^{2-} + Ba^{2+} \rightarrow BaSO_4\downarrow \quad (1)$$

$$RCOO^- + Ba^{2+} \rightarrow P(RCOO)_2Ba \quad (2)$$

$$RCOOH + NH_3{\cdot}H_2O \rightarrow RCOO^- + NH_4^+ + H_2O \quad (3)$$

The most suitable amount of tetradecanoic acid, hexadecanoic acid, and stearic acid to garnered the smallest nanoparticles by the third approach with average size of 25 nm, 20 nm, and 16 nm is 6%-wt, 4%-wt, and 3%-wt, respectively.

Another experiment conducted by Jones *et al.* (2001) shows that both nitrilotriacetic acid (NTA) and nitrilotrimethylenephosphonic acid (NTMP) can be utilized as barium sulfate complexing agents. 0.017 mM NTMP mixed into 0.25 mM $BaCl_2$ and Na_2SO_4 solution in a system with pH of 5.6 would form thin and rounded $BaSO_4$ nanoparticles with NTMP molecule : barium atoms ratio of 1 : 15.[73] Meanwhile, adding 0.078 mM NTA to the same system would produce $BaSO_4$ nanoparticles with NTA molecule : barium atoms ratio of 1 : 3 and morphology transformation at a carboxylate : barium ratio of 1 : 5. NTA performance as a inhibitor shows more particles homogeneity in terms of their monodispersity and adsorption on their surface. In attempt to enhance their beneficial properties, further study was done by Jones *et al.* (2006) to investigate $BaSO_4$ nanoparticles formation involving nitrilotriacetic acid (NTA) in the precipitation process.[74] Based on this study, NTA effectively inhibits barium sulfate precipitation at moderate pH levels, specifically barium complexion below 10% for pH < 7. The morphology transformation of the obtained $BaSO_4$ nanoparticles happens at carboxylate : Ba ratio of 1 : 10 with an average particle size of 208 nm. The presence of NTA increases the induction time of barium sulfate precipitation, suggesting a decrease in nucleation rate, which is likely due to an increase in interfacial free energy.[75] SEM image of $BaSO_4$ in Fig. 6f reveals that the morphology of barite particles synthesized in the presence of NTA exhibits significant alterations as the temperature increases from 25 °C to 60 °C. At the lower temperature, the particles are approximately spherical. However, as the temperature rises, they transform into rhombic shapes, akin to the morphology observed in barite formed under conditions of very low supersaturation.[76] Hence, the optimal temperature for $BaSO_4$ inhibition must be lower than 60 °C.

Aside from the mentioned organic compounds above, ethylenediaminetetraacetic acid (EDTA) also garnered interest of many researchers to facilitate $BaSO_4$ precipitation in order to gain more controlled particle size of $BaSO_4$. EDTA is a water-soluble chleating agent that has high intensity of interaction with metal ions (*i.e.* Ba^{2+}) by using its unique structure which consists of four carboxylate and two amine groups.[77] Li *et al.* (2003) synthesized $BaSO_4$ nanoparticles by mixing 2.19 g of

$BaCl_2$ and 3.21 g of EDTA in 100 mL of distilled water then adding 100 mL of 0.1 mol per L Na_2SO_4 to obtain white $BaSO_4$ precipitate.[43] This precipitation reaction can be described as follows:

$$Ba^{2+} + EDTA \leftrightarrow Ba\text{-}EDTA \quad (4)$$

$$Ba\text{-}EDTA + SO_4{}^{2-} \leftrightarrow BaSO_4 + EDTA \quad (5)$$

The nanoparticles' growth is controlled by forming Ba-EDTA intermediate complex. This intermediate presence would directly reduce free barium ions that can bond with sulfate ion to stabilize the nuclei. EDTA also acts as an inhibitor by building a barrier to ensure the steric hindrance of the nanoparticles in order to prevent agglomeration with steric energy approximately −56.38 kcal mol^{-1}.[78,79] From this experiment, it is concluded that one of the most significant factors in $BaSO_4$ nanoparticles synthesis using EDTA is pH. Reaction with higher pH leads to limitation of free barium ions so that the nanoparticle growth mechanism is more dominant than nucleation.[80] This statement is supported by characterization of $BaSO_4$ nanoparticles obtained from synthesis with EDTA at varying pH using TEM as shown in Fig. 6g–j.

Chen *et al.* (2008) conducted a similar co-precipitation experiment by using 4.0 mmol per L $Ba(NO_3)_2$, 4.0 mmol per L $K_2S_2O_8$ and 8.0 mmol per L EDTA with N_2-bubbling apparatus and γ-ray radiation.[81] The final product is $BaSO_4$ microspheres with an average particle size of 2–3 μm. These microspheres are composed of many quasi-spherical nanoparticles and nanorods. In this precipitation method, water molecules were irradiated so that they generated hydrated electrons, which would reduce peroxydisulfate ion to escalate the sulfate ion rate constant.[10,82] Meanwhile, the barium ion rate constant was tuned by EDTA complex. This result confirms the previous study of $BaSO_4$ nanoparticles precipitation using BaS and Na_2SO_4 as precursor and EDTA as modifying agent.[83] The $BaSO_4$ nanoparticles obtained from this simple direct precipitation have an average size of 16 nm.

Romero-Ibarra *et al.* (2010) developed a novel approach of $BaSO_4$ nanoparticles synthesis with EDTA solvent system and dimethyl sulfoxide (DMSO).[45] The morphology of $BaSO_4$ aggregates varied significantly with pH and EDTA concentration. At pH 4, spherical agglomerates of around 500 nm were observed, while at higher pH, the agglomerate size decreased, and the spherical shape was deconstructed. This phenomenon happens due to EDTA dissociation in a system with high alkalinity, ensuring the surplus of anion for further reaction by surface absorption to increase the intensity of repulsive force, which is beneficial for particle size tuning purposes.[84] It should be noted that the effectiveness of EDTA as a chelating agent can be diminished because of alterations in its pK_a values, since EDTA in a system with low pH are under the influence of carboxylic functional group.[85] $BaSO_4$ synthesis in 5% water–DMSO system in presence of EDTA produces quasi monodisperse fibers with an average diameter less than 200 nm. These observations suggest that water plays a crucial role as a pH buffer in enhancing barium sulfate nanoparticle surface absorption mechanism by EDTA, consequently transforms their morphology from spherical to mesocrystalline fibres.[22] HRTEM images revealed that the fibers are composed of several oriented primary particles, suggesting a hierarchical organization along the [001] and [010] directions. All $BaSO_4$ samples were crystallized in an orthorhombic structure, with crystallite sizes estimated to be about 4 nm for spherical agglomerates and 12 nm for fibres.

Based on this results, Romero-Ibarra *et al.* proposed a mechanism based on multipolar attractions and a brick-by-brick organization of primary particles, facilitated by the preferential adsorption of EDTA on certain surfaces of the $BaSO_4$ nanoparticles as follows:

$$2Cl_{(ac)}{}^{-} + Ba_{(ac)}{}^{2+} + EDTA_{(ac)}{}^{4-} + 2Na_{(ac)}{}^{+} + 2H_{(ac)}{}^{+} \leftrightarrow [Ba\text{-}EDTA]_{(ac)}{}^{2-} + 2Na_{(ac)}{}^{+} + 2Cl_{(ac)}{}^{-} + 2H_{(aq)}{}^{+} \quad (6)$$

$$EDTA^{4\bullet -} + {}_jH^{+} \leftrightarrow H_jEDTA^{4\bullet -j} \quad (7)$$

$$[Ba\text{-}EDTA]^{2\bullet -} + H^{+} \leftrightarrow [BaHEDTA]^{-} \quad (8)$$

$$Ba\text{-}EDTA'_{(aq)} + SO_{4(aq)}{}^{2'-} + 2Na_{(aq)}{}^{+} \leftrightarrow BaSO_{4(s)}\downarrow + EDTA'_{(aq)} + 2Na_{(aq)}{}^{+} \quad (9)$$

The significance of pH value in $BaSO_4$ precipitation with EDTA was later confirmed by further study conducted by Akyol and Cedimagar (2016).[42] Direct precipitation of $BaSO_4$ nanoparticles using $BaCl_2$ and Na_2SO_4 with addition of 0.1 mol per L EDTA in a system with pH = 6 would produces $BaSO_4$ crystals with a mean particle size of 0.44 ± 0.09 μm, relatively smaller than the products gained from the same system with pH = 4 at an average diameter of 0.91 ± 0.36 μm. Further increment of pH value to 8 would results in smaller nanoparticles with an average size of 0.28 ± 0.05 μm. These results is aligned with EDTA tendency to has strong affinity to barium ions and endothermically adsorbed on the particles' surfaces.[86]

2.2 $BaSO_4$ nanoparticles precipitation involving polymers

Aside from organic compounds, many $BaSO_4$ nanoparticles precipitation experiments have been conducted with addition of various polymers. In these experiments, the steric effect of the polymer is mainly used to prevent the reaction of other particles with the nuclei.[87] Qi *et al.* (2000) reported the effects of double-hydrophilic block copolymers to the morphology and size of $BaSO_4$ nanocrystals.[39,88] This synthesis of $BaSO_4$ nanoparticles using 0.5 M $Ba(OAc)_2$, 0.5 M $(NH_4)_2SO_4$, and 1 g L^{-1} of various polymers shows significantly different shape and size. Fig. 7b reveals that poly(methacrylic acid) (PMAA) addition in the system would makes the final product have a rod-like shape with average length of 0.8 μm, composed of 22 nm crystallites due to its carboxylic acid group function hydrogen bond with sulfate ion.[89] These products has significantly different size and morphology compared to non-additive products in Fig. 7a. The modification of polymer to PEG-*b*-PMAA would results in morphology changes to peanut-like shape with particle length of 0.8 m consists of 14 nm crystallites at pH 9 meanwhile

peaches-like $BaSO_4$ particles were obtained with average size of 2 μm composed of 18 nm crystallites at pH 5. Fig. 7c and d show that substituting the polymer to PEG-*b*-PMAA-Asp and PEG-*b*-PEIPA would produce different $BaSO_4$ products consisting of 27 nm and 19 nm crystallites, respectively. The interaction between phosphonate and carboxylic acid group function of PEG-*b*-PMAAP polymer chain leads to stronger $BaSO_4$ nanofibers bonds with length of some tens of micrometers and an average diameter 20–30 nm, as shown in Fig. 7g and h.[90] This morphology variation tendency is related to the bonds between copolymers which would increase in higher pH system owing to the domination of carboxylate groups ionization, hence the increasing repulsive electrostatic bonds.[91] Meanwhile, $BaSO_4$ synthesis with PEG-*b*-PEIPSA produces 10 μm $BaSO_4$ particles with flower-like shape consists of ten petals from secondary crystalline layers. Although the $BaSO_4$ particles is still relatively bigger in size, this discovery becomes the basis for the development of barium sulphate nanoparticles synthesis in the presence of polymer templates. The same research team continued the study of $BaSO_4$ nanofibres synthesis method using PEG-*b*-PMAA-PO_3H_2.[40] SEM and TEM images in Fig. 7e and f shows that $BaSO_4$ synthesis experiment with similar method as their previous study produces long $BaSO_4$ nanofibres which composed of nanofilaments with average diameter 20–30 nm, same as their experiment using PEG-*b*-PMAA. The block structure of PEG-*b*-PMAA-PO_3H_2 improves the stabilization of precursor particles by keeping the binding polyelectrolyte segment distinct from the hydrophilic PEG block core shell.[92] This separation allows each component to perform its specific function more effectively, leading to increased overall stability.

Further experiment conducted by Wang *et al.* (2005) involves a non-ionic block copolymer consists of poly(ethylene oxide) (PEO) and poly(propylene oxide) (PPO), namely PEO–PPO–PEO, to control the crystal growth of $BaSO_4$ nanoparticles.[93] Different amounts of copolymer added to the reactants would generates various shape of $BaSO_4$ particles. $BaSO_4$ precipitates obtained from 1 g per L copolymer have a lamellar star-like morphology with four petals and an average length of 8 μm. On the other hand, $BaSO_4$ precipitates from 2 g per L copolymer solution are obtained in 50 nm square flakes shape. Furthermore, if the copolymer solution concentration increased to 3 g L^{-1}, the obtained $BaSO_4$ particles would be obtained in snowflake-like shape with four main branches, each branches have many twigs with average length around 1 μm. This copolymer-assisted $BaSO_4$ precipitation method involve two important features. The first feature is face-selective adsorption which would makes some face have expanded growth, hence seem longer than the other faces.[94] This phenomenon happens regarding to the different characteristics of the hydrophobic PPO block which by envelops the $BaSO_4$ nuclei to create hydrophobic cores, stimulating the steric effect while the hydrophilic block PEO stretch into the solution, stabilize and maintain the structure of the crystal.[95] The effectivity of this physical adsorption by PEO–PPO–PEO copolymer is highly related to $BaSO_4$ particle size. Smaller particle size would enhance surface area and porosity. Higher porosity implies more spaces within the $BaSO_4$ morphology, leading to faster adsorption rates.[96] The other feature is self-assembled by the copolymer template mechanism itself.[97] The core of the micelles highlighting the PPO block function, effectively inhibits the growth of $BaSO_4$ particles from the core–shell micelles.

Another experiment conducted by Saraya and Bakr (2011) modify $BaSO_4$ nanoparticles obtained from precipitation method with polycarboxylates.[98] In difference from the

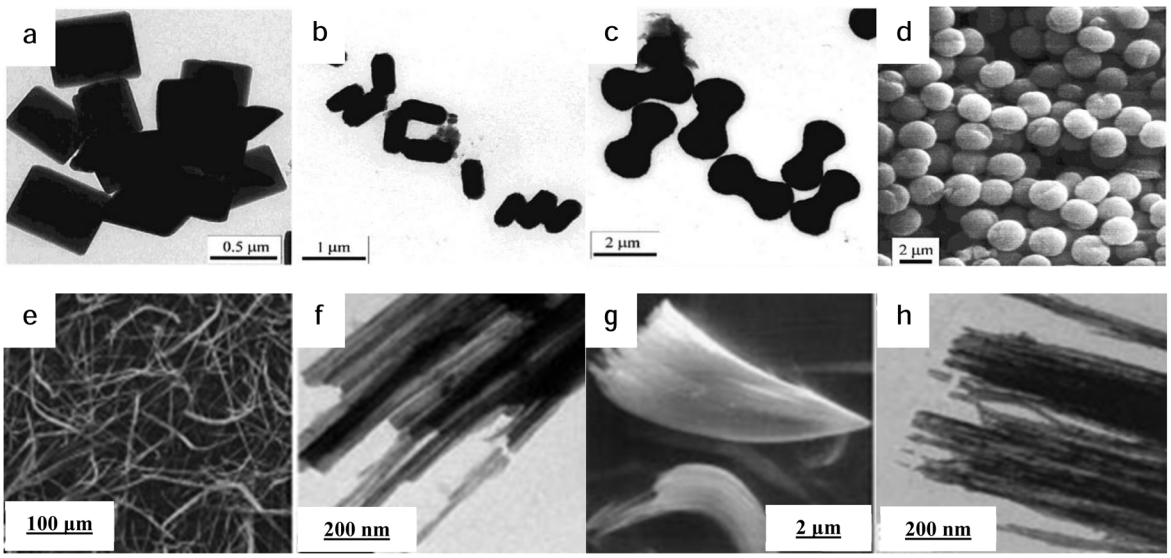

Fig. 7 TEM of $BaSO_4$ particles synthesized in presence of (a) no additives, (b) PMAA, (c) PEG-b-PEIPA, and (d) SEM $BaSO_4$ particles synthesized in presence of PEG-*b*-PMAA-Asp (reproduced from ref. 39 with permission from the American Chemical Society, copyright 2000); (e) SEM and (f) TEM images of $BaSO_4$ particles formed in presence of PEG-*b*-PMAA-PO_3H_2 (reproduced from ref. 40 with permission from Wiley-VCH, copyright 2001); (g) SEM and (h) TEM of $BaSO_4$ fibres and nanofilaments in presence of PEG-*b*-PMAAP (reproduced from ref. 88 with permission from Wiley, copyright 2000).

experiment in the previous study, Saraya and Bakr reacted 0.1 M $Ba(NO_3)_2$ and 0.1 M $(NH_4)_2SO_4$ in a water-soluble organic polymer modifying agent. The obtained $BaSO_4$ nanoparticles have particle size ranging from 6–26 nm, with a mean particle size of 18 nm. The nanoparticles have uniformly elliptical shape with mesopores cavity 6–8 nm in diameter. This unique porous structure of $BaSO_4$ nanoparticles is exhibited due to Ostwald ripening, where the continuous supersaturated condition of the solution, leading to the growth and stabilization of nanoparticles in closed system driven by interfacial energy.[99] The porous structure of nanoparticles also indicates their better dispersibility due to increased surface area, consequently, have more capability to adsorb the modifying agent onto their surface.[100] This result is aligned with the conclusion from the other experiment by Shen *et al.* (2007), which stated that in this precipitation method, polycarboxylate serves as inducer and inhibitor.[71] This experiment was later developed by Nandakumar and Kurian (2012) who synthesized $BaSO_4$ nanoparticles using 3% polyvinyl alcohol (PVA) as a polymeric template.[101] Monodispersed porous spherical $BaSO_4$ nanopowder with low impurity and an average size of 23 nm was achieved according to Scherrer formula at calcination temperature 600 °C. Meanwhile, the calcination at 400 °C still ineffective to gain nanoparticles with high purity whereas calcination at 800 °C leads to excessive agglomeration of $BaSO_4$ nanoparticles since its protective layer already removed from the nuclei.[102] Additionally, $BaSO_4$ obtained from direct precipitation in absence of PVA have higher tendency to agglomerate and developed heterogeneous flaky structure due to higher surface energy and poor solubility.[103]

Later, Sun *et al.* (2014) investigated further the effects of sodium polyacrylate (PAAS) in $BaSO_4$ precipitation reaction.[104] The initial intermediates were still in enourmous particles before gradually reduced to spherical particles with a mean particle size of 200 nm. Further precipitation would increase the nanoparticles' growth to 20 nm. The final products were obtained with an average size around 30 nm and satisfactory dispersity. As confirmed in previous study, PAAS would emits polyacrylate ions that reacted with barium ion *via* ionic bonding, forming barium polyacrylate intermediate.[40] Since the intermediate is more soluble in water than PAAS owing to its chain length and weight fraction, the reaction system materialised in form of suspension.[105] Then, the sulfate ion from ammonium sulfate addition into the suspension would bonds with free barium ion to form $BaSO_4$. As the precipitation time elapses, the intermediates are slowly dissolved so that nanoparticle growth can occur. The released polyacrylate ions would rearranged as an adlayer to inhibit the agglomeration of $BaSO_4$ nanoparticles.[106]

Zhao and Liu (2006) analyzed $BaSO_4$ nanoparticles obtained from precipitation method by using 0.1 grams of sodium hexametaphosphate ($(NaPO_3)_6$) as stabilizer, BaS and Na_2SO_4 as main reactants.[83] The result shows that $BaSO_4$ nanoparticles obtained from synthesis with $Na(PO_3)_6$ have bigger average size of 203 nm, indicating weaker influence to inhibit the growth of nanoparticles. However, Gupta *et al.* (2010) got different outcomes by dissolving 10 grams of $Na(PO_3)_6$ in 80 mL before mixed with 10 mL of 1 M Na_2SO_4 and 10 mL of 1 M $Ba(NO_3)_2$ solution.[107] The obtained $BaSO_4$ precipitates size is around 30–55 nm. This difference pinpoints the importance of determinating the amount of modifying agent involved in synthesis to gain the optimal size of nanoparticles.

2.3 $BaSO_4$ nanoparticles precipitation involving surfactants

$BaSO_4$ nanoparticles precipitation also has been experimented by adding surfactants, either the non-ionic or ionic surfactants. The interest of this experiment is increasing owing to the hydrophilic and hydrophilic configuration in surfactant that can be utilized to control the growth of nanoparticles.[108] Li *et al.* (2011) investigated in influence of dodecyltrimethylammonium bromide (DTAB) to morphology and particle size of $BaSO_4$ synthesized with direct precipitation method using $BaCl_2$ and Na_2SO_4 as precursor.[44] The $BaSO_4$ precipitates obtained from a synthesis without DTAB have four-leaves-shaped morphology with an average size of 4.85 μm. As the concentration of DTAB is increased to 10.0 mmol L^{-1}, flower-shaped structures with petals begin to form with an average dimension of 180 nm × 100 nm. Increment of DTAB concentration to 12.5 mmol L^{-1} would produce flower-like aggregates composed of nanorods with a mean particle size about 190 nm length and 80 nm width. Further addition of DTAB concentration to 15.0 mmol L^{-1} would result in aggregates with eight petals flower-shaped morphology. Each petals have a mean size of 1.15 μm × 1.00 μm. Synthesis of $BaSO_4$ with 25 mmol per L DTAB would produces similar aggregates to the one obtained in absence of DTAB with size reduction to 3 μm. Based on this experiment, Li *et al.* proposed a two-step $BaSO_4$ nanoparticles growth mechanism. The first step is the formation of $BaSO_4$ nuclei and DTAB adsorption to the surface of $BaSO_4$ crystals which increased by increasing electrostatic interaction frequency of the positive charge carried by the polar head groups DTAB and sulfate anions.[109] The second step is the construction of a flower-shaped structure using the formed nanorods. Meanwhile, another experiment conducted by Jha *et al.* (2019) using cetyltrimethylammonium bromide (CTAB) proves its less effectiveness to control $BaSO_4$ particles size as concluded from their mean particle size of 98.12 nm.[38] This statement is supported by previous study by Zhao *et al.* (2011) which shows that the presence of CTAB in the ion-exchange reaction between solid-state barium carbonate ($BaCO_3$) and aqueous sodium sulfate (Na_2SO_4) had a minimal impact on the morphological control of the resulting $BaSO_4$ crystals.[110] The formation schemes of $BaSO_4$ nanoparticles with several DTAB concentrations are shown in Fig. 8.

Octadecyl dihydrogen phosphate (*n*-$C_{18}H_{37}OPO_3H_2$, ODP), another surfactant was proposed by Bala *et al.* (2006) as a modifying agent in $BaSO_4$ precipitation method.[111] The liquid solvent medium was prepared by dissolving ODP to 0.1 M KOH before mixed with 20 mL 0.5 M $BaCl_2$. 20 mL 0.5 M $(NH_4)_2SO_4$ then added dropwise into the solution. The end product garnered from this precipitation reaction with weight ratio of ODP/$BaSO_4$ 2%-wt is spherical with an average size of 76 nm. These nanoparticles are equipped with core–shell structured

protective layer (barium alkyl phosphates, Ba-ODP or Ba-2ODP) with thickness about 3–8 nm and cavities with an average diameter approximately 5–16 nm. This method is proven to successfully modify the surface tension of $BaSO_4$ nanoparticles with ODP amount above 1.85%-wt to make it more hydrophobic. The modifying mechanism can be estimated by FTIR analysis data that the P–OH bonds is only detected in ODP spectra, which means that the barium ion reacts with ODP, producing hydrophobic salt to enhance the surface tension of nanoparticles.

Li *et al.* (2012) had used different approach to precipitate $BaSO_4$ nanoparticles in presence of dodecyl benzene sulfonic acid (DBSA) in ethanol–water system with $BaCl_2$ and Na_2SO_4 as precursor.[112] The addition of 1%-wt DBSA is proven to decrease particle size drastically from 1000 nm to 56 nm. Further increment of DBSA concentration to 5%-wt would produces well-dispersed rounded 46 nm nanoparticles. The products with higher DBSA composition (5%-wt) have higher total weight loss about 6.32%-wt due to decomposition of DBSA at an optimal temperature of 454 °C. This data implies that further addition of DBSA would results in thermal instability of obtained $BaSO_4$ nanoparticles. The summary of raw materials and additives used for $BaSO_4$ nanoparticles synthesis and the mean particle size produced from several studies is listed in Table 1. The evaluation of each additive's advantages and setbacks in barium sulfate nanoparticles precipitation is presented in Table 2.

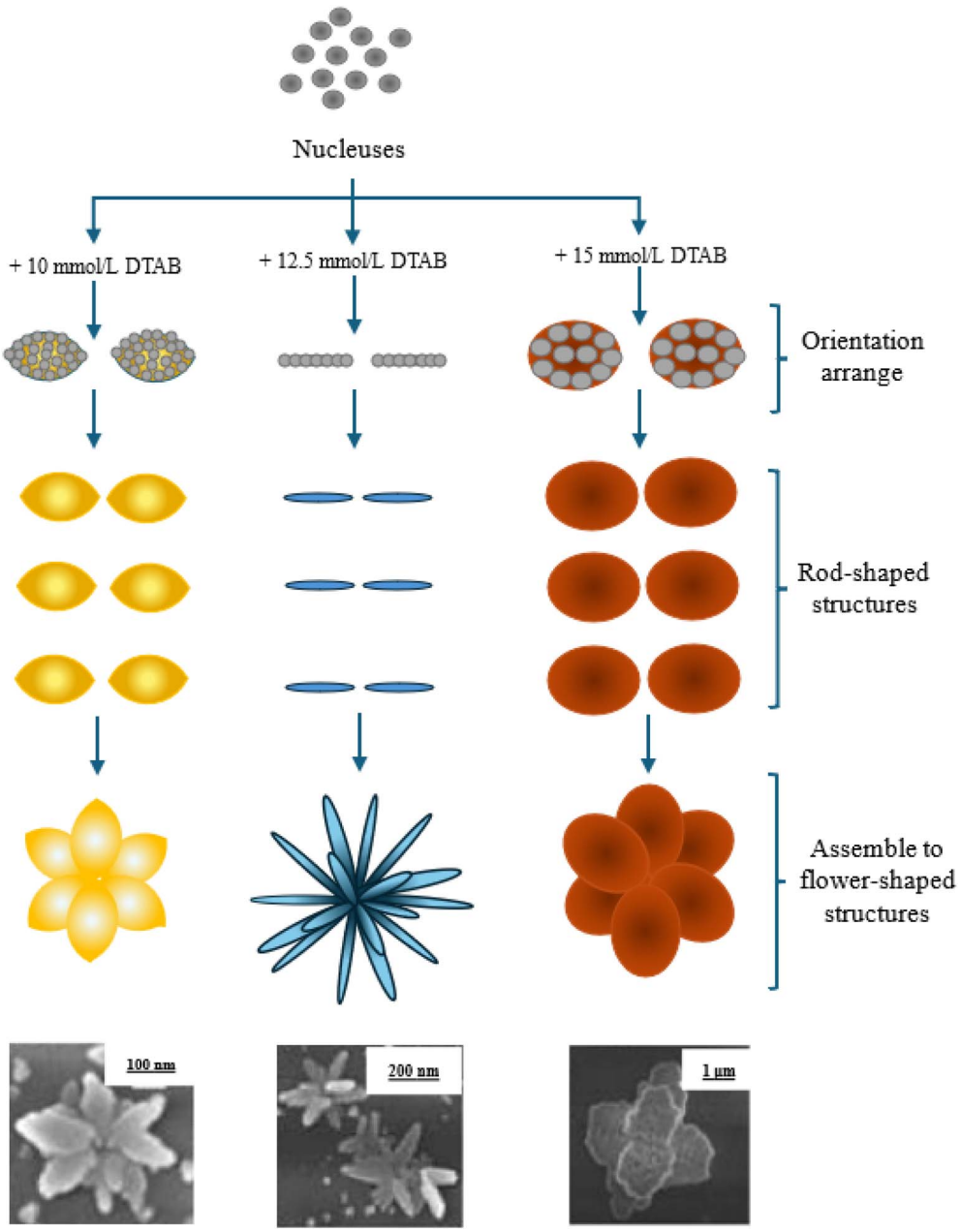

Fig. 8 $BaSO_4$ nanoparticles growth mechanism with different DTAB concentration.

Table 1 Lists of raw materials and particles size gained from $BaSO_4$ nanoparticles precipitation

Main reactants (precursors)	Solvent	d_{50} (nm)	Ref.
$BaCl_2$, $(NH_4)_2SO_4$	Ethanol	36	59
$BaCl_2$, $(NH_4)_2SO_4$	Ethanol–water	54	62
$BaCl_2$, Na_2SO_4	Water–benzene	35.995	63
$Ba(NO_3)_2$, Na_2SO_4	Water–THF	67	65
$BaCl_2$, Na_2SO_4	Ethanol–water in presence of stearic acid	16	71
$BaCl_2$, Na_2SO_4	NTMP	N/A	73
$BaCl_2$, Na_2SO_4	NTA	208	74
$BaCl_2$, Na_2SO_4	Water + EDTA	13	43
BaS, Na_2SO_4	Water in presence of $Na(PO_3)_6$	203	83
$Ba(NO_3)_2$, Na_2SO_4	Water in presence of $Na(PO_3)_6$	30–55	107
$Ba(NO_3)_2$, $K_2S_2O_8$	Water + EDTA	2×10^3, consists of quasi-spherical and rod-like nanoparticles	81
$BaCl_2$, Na_2SO_4	Water–DMSO in presence of EDTA	4 (nanospherical), 12 (nanofibers)	45
$BaCl_2$, Na_2SO_4	Water–EDTA	280	42
$BaCl_2$, Na_2SO_4	Water in presence of DTAB	190×80	44
$BaCl_2$, Na_2SO_4	Water in presence of CTAB	98.12	38
$BaCl_2$, $(NH_4)_2SO_4$	Water in presence of ODP	76	111
$BaCl_2$, Na_2SO_4	Ethanol–water in presence of DBSA	56	112
$Ba(NO_3)_2$, $(NH_4)_2SO_4$	Water in presence of polycarboxylates	18	98
$BaCl_2$, $(NH_4)_2SO_4$	Water in presence of PVA	23	101
$BaCl_2$, $(NH_4)_2SO_4$	Water–PAAS	~30	104
$BaCl_2$, Na_2SO_4	Water–PEO–PPO–PEO	50	93
$Ba(OAc)_2$, $(NH_4)_2SO_4$	PMAA	22 (primary crystallites)	88
$Ba(OAc)_2$, $(NH_4)_2SO_4$	PEG-*b*-PMAA	14 (primary crystallites)	88
$Ba(OAc)_2$, $(NH_4)_2SO_4$	PEG-*b*-PMAA-Asp	19 (primary crystallites)	88
$Ba(OAc)_2$, $(NH_4)_2SO_4$	PEG-*b*-PEIPA	27 (primary crystallites)	88
$Ba(OAc)_2$, $(NH_4)_2SO_4$	PEG-*b*-PMAAP	20–30 (nanofibres)	88
$Ba(OAc)_2$, $(NH_4)_2SO_4$	PEG-*b*-PMAA-PO_3H_2	20–30 (nanofibres with an average length of several hundred micrometers)	39 and 40

2.4 $BaSO_4$ nanoparticles precipitation involving ionic liquid

Ionic liquid is a salt solution formed by combining organic cations and organic or inorganic anions with relatively stable liquid properties at room temperature.[113] Ionic liquids also have a remarkable ability to resist external forces and enhance catalytic processes due to their high conductivity and viscosity. The heat-resistant and electrical conductivity properties qualified ionic liquids application in proton exchange membrane fuel cells in order to enhance its durability and power density up to 500 kW by altering the IL's structure with a template to create

Table 2 Comparison of $BaSO_4$ nanoparticles precipitation involving organic compounds, polymers, and surfactants

	Advantages	Setbacks
Organic compounds	• Organic capping agents control particle size, spheric morphology, and improve dispersion effectively by forming protective layers or steric hindrance • Fine-tuning of nanoparticle size can be done simply by solvent composition or pH adjustments	• The vast choices of organic compound can impacts particle morphology, different kind of organic compound would produces irregular shaped nanoparticles • High pH systems for several organic acids can lead to sporadic and uneven particle growth due to limited barium ion availability
Polymers	• Different polymer types offer a wide range of size and morphology control, such as rod-like, blocks, or flower-shaped structures • Polymers-based agents would produce nanoparticles with uniform sizes and porous structures	• High polymer concentrations may lead to excessive stabilization, hindering controlled growth • Some polymers performance is highly dependent to pH and temperature. This can result in inconsistent particle size • Limited availability
Surfactants	• Surfactants can improve control over nanoparticle size and structure through selective surface adsorption • Surfactants in certain concentration can affects the hydrophilic or hydrophobicity of the system to enhance nanoparticles' dispersibility	• The thermal stability of the product is highly affected by surfactant's concentration in the system • Ionic surfactants are more likely exhibit less control over particle size and morphology compared to non-ionic surfactants

protic ionic liquid (PIL) polyelectrolyte, which has excellent thermal stability and higher proton conductivity.[114]

The cationic proton head and anionic alkyl chains of ionic liquid have distinct characteristics at microscopic scale. With their long alkyl chains, ionic liquids emphasize their hydrophobic features and improve the dissolution of nanoparticles precursors, thereby increasing their thermal stability. Hence, some ionic liquids can act as stabilizers to improve the performance and stability of a nanomaterial.[115] The hydrophobic properties have become a key factor in the development of microwave-assisted ionic liquid synthesis method, which is used to produce corrosion inhibitors and solvents for biomass conversion.[116] Meanwhile, in general, the hydrophilic head group influences solubility and surface activity of the micelles in the solution.[117,118]

Ionic liquid has gained interest as a green solvent for its high solubility in water and thermal properties.[119] Hence, many researchers have developed various synthesis route using this relatively new and non-toxic solvent for many purposes, including the utilization of environment-friendly IL-based electrolyte with wide electrochemical window in supercapacitor energy storage system, lignocellulosic biomass conversion in presence of 1-alkyl-3-methyl imidazolium-based IL as green catalyst, reuseable green solvent and catalyst for plastic degradation process in relatively low heat, green IL-based corrosion inhibitor with simple manufacturing method, and effective solvent system in synthesis of nanoparticles.[120–124]

Kowacz *et al.* (2011) analyze the most probable mechanism of $BaSO_4$ nanoparticles synthesis using precipitation method with various ionic liquids and its effects on the crystallization process.[125] In this study, $BaSO_4$ precipitation was carried out by mixing 5 mL solution consists of 0.04 M Na_2SO_4 and 0.05 M of ionic liquid with 100 μL of 0.1 M $BaCl_2$ in a reactor, then quickly quenched after the mixture is in highly saturated state. Based on this experiment, $BaSO_4$ nanoparticles size in different ionic liquid has significantly dependent to their electrical conductivity and diffusivity in water. Therefore, ionic liquid viscosity is also closely related to the obtained $BaSO_4$ nanoparticle size and diffusion coefficient according to Stokes–Einstein equation for mass transfer.[126] Usually, nucleation kinetics correlate with the diffusion of constituent units, and according to Stokes' law, higher viscosity slows the mobility (μ) of charged particles.[127] However, the experimental data revealed that the nucleation rate of ionic crystals increased with arising solvent viscosity, as shown in Fig. 9a and b, thus this phenomenon contradicts Stokes' law and the conventional colloidal system crystallization.

The diffusion rate of the barium and sulfate ions needed to ensure $BaSO_4$ nucleation is directly dependent on the frequency of water exchange in the solution interface, which increased by electrostatic attraction and solute's affinity dependent to its polarity in the water–IL system.[128,129] Since this reaction happen in an ionic liquid system, the attraction between water's partial charge and ions from IL compound would decrease the water molecules' potential energy. The hydrophilic nature of ILs causes them to disrupt the cohesive forces of water and bind its molecules to $BaSO_4$ particles, which leads to a higher rate of

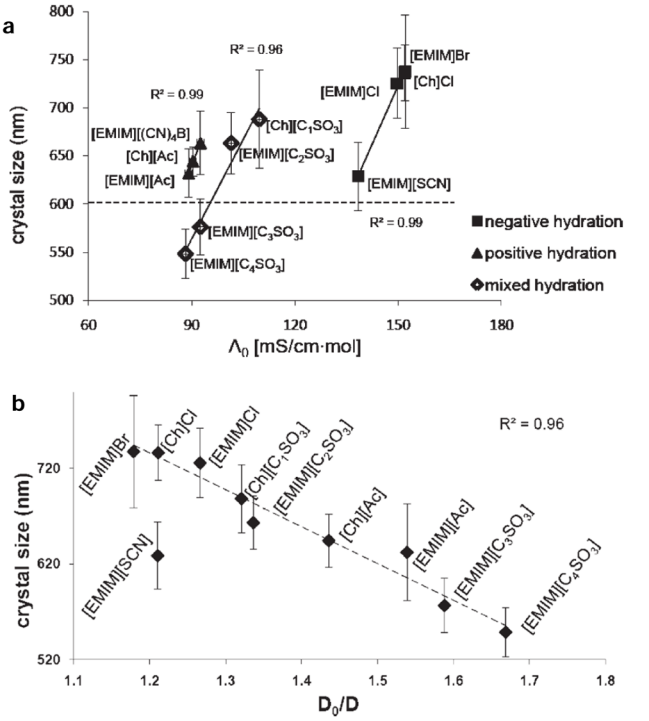

Fig. 9 Correlation curve between $BaSO_4$ crystal size and (a) limiting molar conductivity (Λ_o); (b) diffusion in water (D_o/D) (reproduced from ref. 125 with permission from the American Chemical Society, copyright 2011).

diffusion.[130] This condition would ensure the stabilization of the solution and consequently increase the residence time of the reaction. Conversely, hydrophobic feature of IL would enhance the reactivity of hydroxide group in order to support the release of water molecules and the separation of precipitate.[131]

The solution stability degree relies on background ions dipole moment distribution in the solution.[132] Closer ions have less impactful electric fields, thus reducing their influence on the water molecules. Moreover, the dynamic between hydrophilic ions and hydrophobic ions would significantly influence the movements of water molecules. Positive hydration occurs when ions have a strong affinity for water molecules so that they overcome the water cohesion, creating a hydration shell around them.[133] This ions is generally known as hydrophilic ions. Positive hydration mechanism would result in a more ordered water shell around the ion, which limits the mobility of water molecules. On the other hand, negative hydration occurs when ions have a weaker affinity for water molecules compared to water cohesion in the vicinity of sufficiently large single-charged ions, hence increases the water molecules mobility.[134] This effect is observed when hydrophobic alkyl chains attached to imidazole rings reduce interactions with polar surface sites due to their nonpolar nature. These hydrophobic chains promote the formation of a more compact, water-repellent layer on the metal surface, thereby enhancing its corrosion inhibition efficiency.[135]

Table 3 Characteristics of ILs used for $BaSO_4$ nanoparticles synthesis ($T = 25$ °C)

ILs					
Cations	Anions	Chemical structure	ρ (g cm^{-3})	μ (cP)	Ref.
$[EMIM]^+$	$[(CN)_4B]^-$	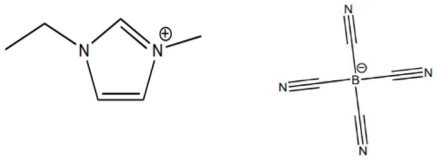	1.0363	19	125, 138 and 139
$[EMIM]^+$	$[Ac]^-$	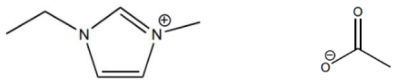	1.03	91–162	125 and 140
$[Ch]^+$	$[Ac]^-$	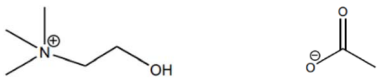	0.995	55.6 (in CH_3COOH with molar ratio of 1 : 2)	125, 141 and 142
$[EMIM]^+$	$[SCN]^-$	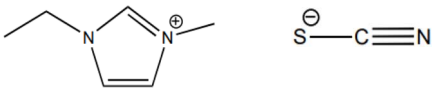	1.1162	22	125, 138 and 139
$[EMIM]^+$	Br^-	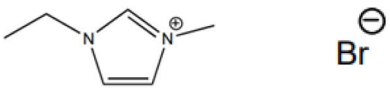	1.48	N/A	125 and 139
$[EMIM]^+$	Cl^-	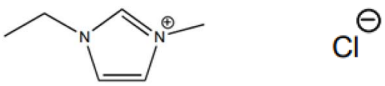	1.186	3530	125 and 139
$[Ch]^+$	Cl^-	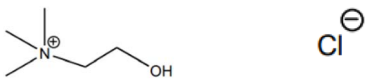	1.103984 ($ChCl/2H_2O$, 100 wt%)	37.760 ($ChCl/2H_2O$, 100 wt%)	125 and 143
$[Ch]^+$	$[C_1SO_3]^-$	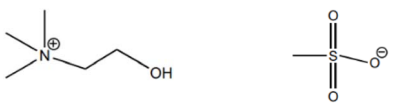	N/A	N/A	125
$[EMIM]^+$	$[C_2SO_3]^-$	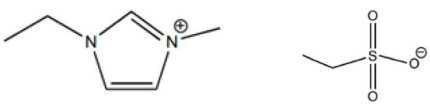	1.203	200	125 and 144
$[EMIM]^+$	$[C_3SO_3]^-$	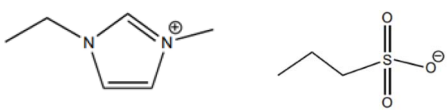	N/A	N/A	125
$[EMIM]^+$	$[C_4SO_3]^-$		N/A	N/A	125
$[3,4\text{-DCBSMIM}]^+$	Cl^-	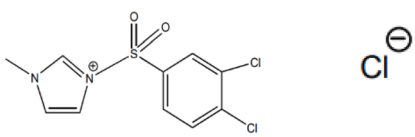	N/A	N/A	102
$[(MIM)C_2COOH]^+$	Cl^-	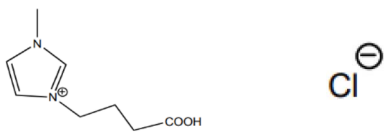	N/A	N/A	46

The other parameter correlated to the obtained $BaSO_4$ particle size is electrical conductivity. The conductivity of an electrolyte solution is determined by diffusion of ions, as described by the Nernst–Einstein equation.[136] However, at higher concentrations, the tendency of ions association can lead to the formation of neutral droplet, thus lowers the electrical conductivity.[137] The experiment results indicated that the increment of solvent viscosity and the association of IL ions in a solution environment enhance the nucleation rate, leads to higher conductivity and smaller final products. The charge density of these ILs is strongly related to hydration enthalpy. Hydrogen enthalpy is the combination of ligation enthalpy and dispersion enthalpy.

The effect of ILs on barite nucleation follows different trends based on the hydration characteristics of the IL anions. ILs with negatively hydrated anions like $[SCN]^-$ and halides (Cl^-, Br^-) show a trend with crystal size around 620–750 nm and the conductivity approximately ranging from 130–170 mS cm^{-1} mol^{-1}, while those with positively hydrated anions like $[Ac]^-$ and tetracyanoborate $[(CN)_4B]^-$ show another trend with crystal size around 620–670 nm and smaller conductivity around 90–120 mS cm^{-1} mol^{-1}. Sulfonate anions, which have mixed hydration properties, define an intermediate trend between the positive and negative hydrated anions. In solutions of ILs with anions of mixed hydration characteristics, two distinct regimes can be distinguished with respect to the effect on barium sulfate nucleation. ILs with longer chains (C3–C4) have smaller particle size compared to the nuclei formed in ILs with positively hydrated anions. This suggests that the net hydration of the anion is dominated by the hydrophobicity of the carbon chain in the C3–C4 region. The smallest particle size of $BaSO_4$ from precipitation is achieved by using $[EMIM]C_4SO_3$. A more advanced synthesis of $BaSO_4$ nanoparticles with IL [3,4-DCBSMIM]Cl and $Ba(NO_3)_2$ using solution combustion system (SCS) in a muffle furnace preheated at 400 °C results in much smaller $BaSO_4$ particles with an average size approximately 11.6 nm.[21] In addition, $BaSO_4$ nanoparticles synthesis can also gained from robust precipitation with 0.56 gram $Ba(NO_3)_2 \cdot 2H_2O$ in 40 mL H_2O and 4 M NaOH as main reactant and 0.05 gram monocationic IL $[(MIM)C_2COOH]Cl$ in 10 mL pure water as capping agent.[46] This solution is added by 0.27 gram of ammonium persulfate in 30 mL pure water as reaction initiator. This synthesis would produced porous fish-skeleton like $BaSO_4$ nanostructure which has excellent characteristics to paired with poly aminophenol (POAP) to create nanofillers for supercapacitors. The additional information about physical properties of ILs used in barium sulfate nanoparticles synthesis are provided in Table 3.

3. Synthesis of $BaSO_4$ nanoparticles in modified reactors

Although the synthesis of nanoparticles *via* chemical precipitation is the easiest to scale up for industrial production, the use of conventional stirring methods suffers from large and widely distributed particle sizes due to poor macromixing and micromixing efficiency which is vital in providing the necessary supersaturated conditions.[145] Therefore, several modifications to the reactor technology were developed to support the production needs on an industrial scale while improving the homogeneity and dispersion of nanoparticles that significantly affect the final product yield. A couple of factors that can be observed in nanoparticle reactors are flow rate, stirrer rotation speed, and the operating temperature inside the reactor vessel.

3.1 Rotating packed bed (RPB) reactor

Packed bed reactor, also known as fixed bed reactor, is a column containing catalysts or packing in a solid phase with well-distributed shape and size. These packings usually are utilized to provide contact in a chemical process, usually between gas–liquid, vapor–liquid, and liquid–liquid phase.[146] This unit can be enhanced by modifying it with a rotating device to enhance overall efficiency of the process, mainly to reduce

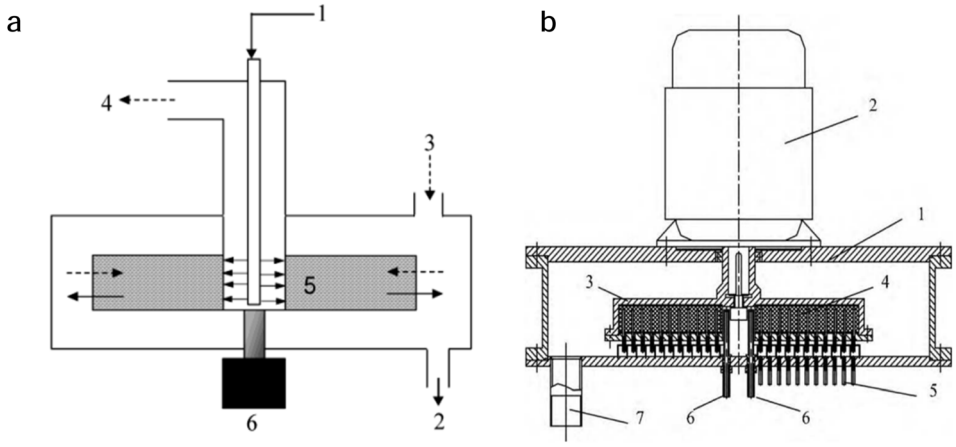

Fig. 10 (a) Sketch of horizontal-axis RPB (consists of: (1) liquid feed inlet; (2) liquid outlet; (3) vapor inlet; (4) vapor outlet; (5) packing; (6) motor) (reproduced from ref. 149 with permission from the American Chemical Society, copyright 2004); (b) sketch of RPB with radial sampling tubes (consists of: (1) shell; (2) electrical motor; (3) rotor; (4) packing; (5) sampling tubes; (6) liquid inlets; (7) liquid outlet) (reproduced from ref. 152 with permission from Elsevier, copyright 2010).

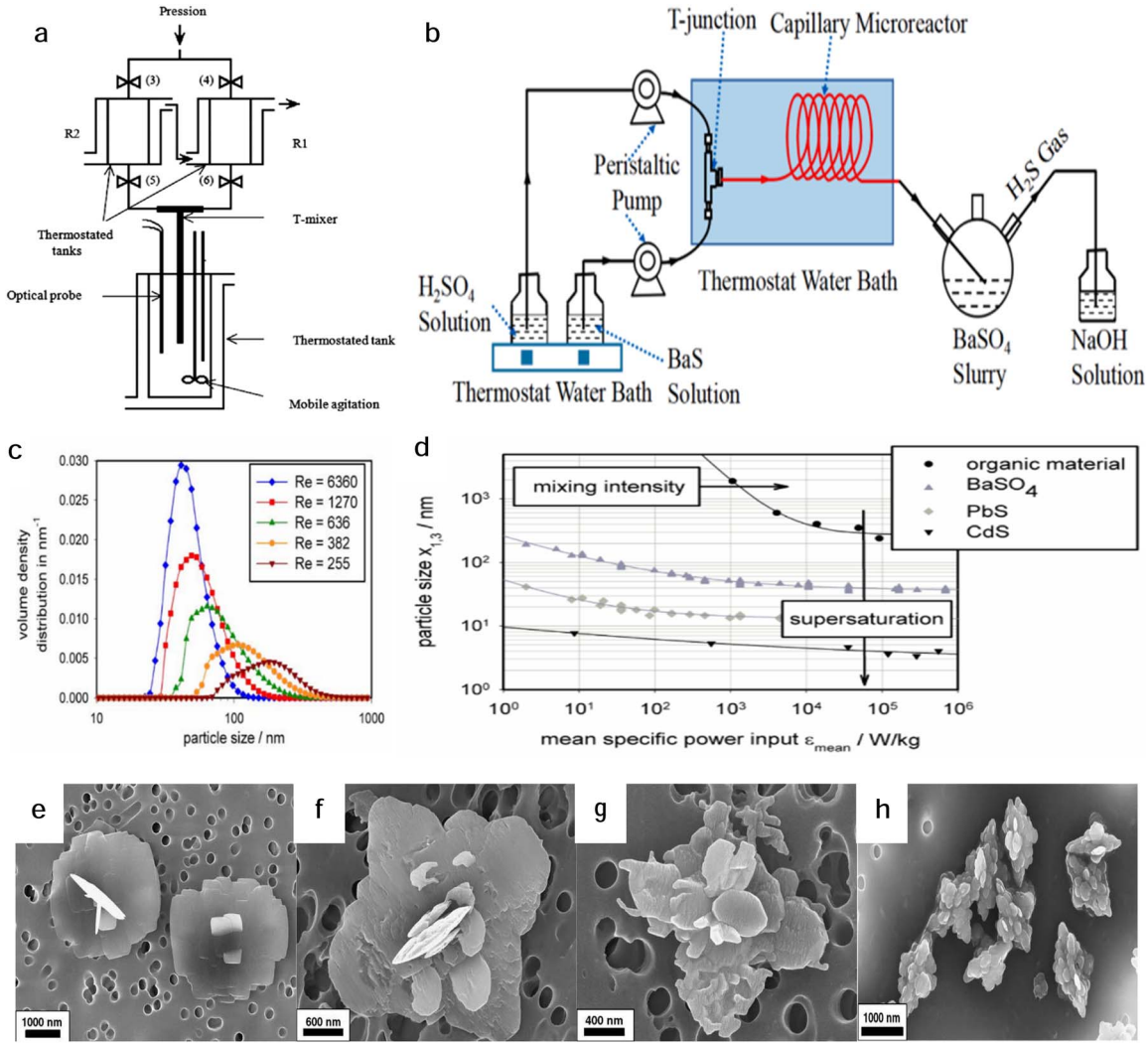

Fig. 11 (a) Sketch of a T-mixer reactor (reproduced from ref. 171 with permission from Springer, copyright 2019); (b) scheme of a modified T-mixer reactor with a capillary microreactor for microflow precipitation of $BaSO_4$ nanoparticles (reproduced from ref. 32 with permission from Elsevier, copyright 2023); (c) correlation curve of volume density distributions of $BaSO_4$ nanoparticles and particle size at various Reynold number and (d) correlation curve of $BaSO_4$ nanoparticles size and power input of T-mixer reactor (reproduced from ref. 159 with permission from Springer, copyright 2010); particle morphology of precipitated barium sulfate with Y-mixer at Sa = 350 and initial free lattice ion ratios (R): (e) R = 0.1, (f) R = 1, (g) R = 10, and (h) R = 100 (reproduced from ref. 72 with permission from Elsevier, copyright 2006).

the required size of the reactor needed in production system while also increase the gravitational force by tuning its angular velocity.[147,148] In nanoparticle preparation method using RPB, the precursors flows through the rotor's inner cavity before sprayed using nozzle on the inner edge of the rotor. This process would make the small droplets of reactants contacts easier due to the increasement of surface area.[149] The liquid is contacted with porous packing to ensure the dispersion and optimal mass transfer in the reactor.[150] As a result, the final products would be more homogeneous in terms of the size and morphology of the nanoparticles. The design of horizontal RPB and modified RPB can be seen in Fig. 10a and b, respectively.

An experiment conducted by Fang *et al.* (2021) using $BaCl_2$ solution and a mixture of methanol and H_2SO_4 on an RPB with a speed of 1500 rpm and a component flow rate of 300 mL min^{-1} under operating temperature conditions of 60 °C was able to produce $BaSO_4$ nanoparticles with an average diameter of 13 nm.[48] Meanwhile, the $BaSO_4$ nanoparticle synthesis process carried out at rotational speeds of 500 rpm and 2500 rpm produced particles with a diameter of 17 nm and 10 nm, respectively. Thus, an increase in RPB rotational speed is inversely proportional to particle growth. A similar statement was made in the experimental results of $CaCO_3$ nanoparticle synthesis with a rotating fluidised bed.[151] They state that to produce smaller nanoparticles with large interparticle cohesive forces, higher rotational speeds are required to overcome these forces and achieve effective fluidization. Other experiments conducted by Yang *et al.* (2010) also led to the conclusion that the decreased growth of $BaSO_4$ nanoparticles in RPB is due to the greater centrifugal force that increases the relative velocity between the nozzle and packing flow.[152] As a result, there is an increase in micromixing efficiency and homogeneous supersaturation conditions occur in the RPB reactor.

3.2 T-Mixer and Y-mixer reactor

T-Mixer is a type of fluid mixing device where two liquid streams meet at a T-junction. T-mixer consists of two inlet streams and single outlet stream, as shown in Fig. 11a. The mixing process involves the injection of a solution containing a dissolved substance through one inlet and a liquid antisolvent through the other inlet.[153] The two liquid streams meet at the T-junction, resulting in planar, swirling folds and simultaneously causing fluid turbulence as the Reynolds number increases.[154] This process allows for efficient mixing of the two liquids as well enhancing the mass transfer, increase reaction rate and higher selectivity. T-mixers can be scaled up or down, depending on the specific requirements of the synthesis process. This advantages makes them versatile tools for both laboratory and industrial applications.[155,156]

Driven by its versatility, there have been several studies on the precipitation of $BaSO_4$ nanoparticles using a T-Mixer reactor. The study on the synthesis of $BaSO_4$ nanoparticles using a T-Mixer reactor conducted by Schwarzer and Peukert (2002) analyzed the precipitation results from the reaction of $BaCl_2$ and H_2SO_4 at a constant temperature of 25 °C.[157] The results of the study showed that an increase in the inlet flow rate and an increase in the rotation speed per minute would trigger a driving force in the form of ionic supersaturation of dissociated barium and sulfate ions, as illustrated in Fig. 11d. This condition is corresponds to the Von-Weimarn rule which states an inverse relationship between supersaturation level and particle size.[158] The smallest product size was obtained at a flow rate of 5 mL s^{-1} with a diameter of about 80 nm. This phenomenon directly affects the nucleation rate and growth of nanoparticles, so the size of the monocrystalline precipitate becomes smaller with the increase in rotation speed. However, during this precipitation process, agglomeration occurs, which can hinder the optimization of the barium sulfate nanoparticle size. Further study proceeded by Gradl and Peukert (2010) were carried out with initial feed concentration of 0.5 M $BaCl_2$ and 0.33 M H_2SO_4 in a T-mixer constructed of two feed tubes of 0.5 mm and pressure drop along the pipeline is kept constant.[159] Correlation graphs in Fig. 11c show that the size of $BaSO_4$ nanoparticles decreased with the increase of Reynold's number. This trends occur due to variable of nucleation rate and growth of nanoparticles as a function of solubility and interfacial tension.[160] Supersaturation condition of $BaSO_4$ triggers the nucleation rate to be higher than the growth rate.[161] This condition implies that smaller nanoparticles can be obtained by installing the T-mixer with higher power input intensity to increase the feed flow rates and consequently optimize the liquid–liquid contact frequency.

Similar results were obtained based on further research by Pieper *et al.* (2011) with $BaCl_2$ reactants that were combined with dispersing agent Melpers 0030 before reacted with K_2SO_4 in a T-Mixer reactor.[162] The 30%-wt dispersing agent played a role in preventing agglomeration that could occur during the continuous precipitation reaction. Experimental results at various reactant flow rates showed a similar trend to the findings of Schwarzer and Peukert,[157] with the residence time decreasing as the Reynolds number increased. Additionally, an increase in supersaturation with the addition of reactant concentration significantly shortened the residence time, from 24 ms to 1.66×10^{-2} ms for reactant concentrations of 0.05 mol L^{-1} and 0.128 mol L^{-1}, respectively. This condition causes particles to easily undergo nucleation. However, further increasing the reactant concentration to 0.25 mol L^{-1} was less effective in reducing particle size. The increment of operating temperature during nanoparticle synthesis resulted the increasing diffusion coefficient in water, indicating that inhibition of nanoparticles growth is more likely to happens at lower temperatures.[163] The optimal size of barium sulfate nanoparticles from this experiment was obtained at 105 nm at a temperature of 20 °C with a flow rate of 900 mL min^{-1}. Meanwhile, the concentration of the antisolvent not significantly affect particle size obtained from this experiment. Thus, small-sized $BaSO_4$ nanoparticles can be obtained by increasing the mixing rate and lowering the temperature to support nucleation in this condition.

Another experiment performed by Kockmann *et al.* (2008) suggests a convective mixing precipitation method simulation model by using a T-Mixer reactor, 0.5 M $BaCl_2$ and 0.33 M H_2SO_4 as reactants, combined with diffusive transport and thermodynamic precipitation theory.[164] This experiment shows the importance of Reynold number, which must be higher than 350 for the condition above to ensure nanoparticle synthesis with particle size lower than 100 nm. Similar results is gained through an experiment of barium sulfate nanoparticle synthesis using Y-mixer with supersaturation level at 350 and free lattice ion ratio ranging from 0.1 to 100.[72] Y-Mixer also provides efficient mixing, but it may not be as effective as the T-mixer in certain situations. Y-Mixer can create a more complex flow pattern, which leads to better mixing in some cases but may also introduce additional turbulence, potentially affecting nanoparticle synthesis due to the occurrence of stagnant region.[165,166] At first, suspension with $R < 1$ indicates heterogenous nucleation with two peaks of particle size distribution. These peaks would gradually diminished into a monomodal curve with mean particle size approximately 1–1.6 μm due to aggregation prevention by repulsive electrostatic forces caused by the adsorption of barium ions on the particles' surface.[167] SEM images in Fig. 11e–h reveals that the morphology of $BaSO_4$ nanoparticles changes from nearly rectangular at a low R value to star-shaped at $R = 1$ and 10, and to a fir cone-like shape at $R =$ 100.

Zhang *et al.* (2023) modified the conventional T-mixer reactor by combining it with a spiral capillary microreactor with an inner diameter of 0.8 mm at the outlet stream to enhance the quality of the final product.[32] The modified reactor configuration is illustrated in Fig. 11b. This experiment uses BaS and H_2SO_4 with an initial concentration of 1 M for both feed material and 5 M NaOH was utilized to absorbed the exhausted H_2S gas, a by-product from this reaction. The result shows a similarity with previous studies that the increment of Reynold number from 41.8 to 664 would decrease the particle size from 53.5 nm to 35.7 nm due to intensified heat and mass transfer.[168] Meanwhile, the increment of residence time would decrease the

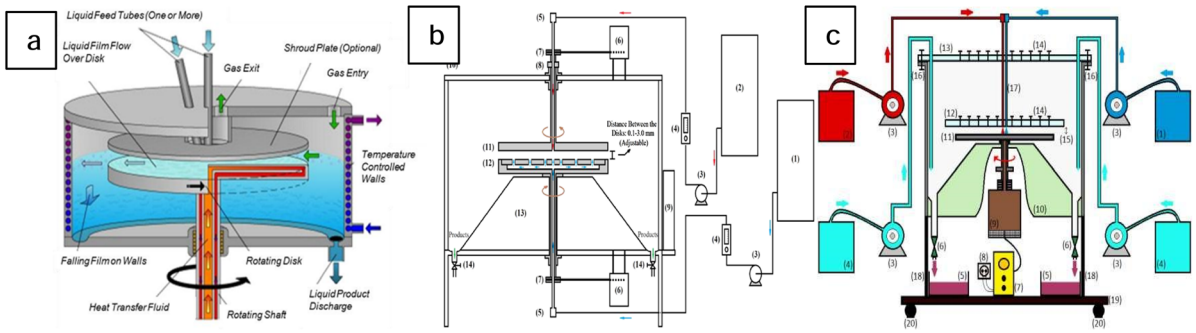

Fig. 12 Scheme of (a) spinning disc reactor (SDR) (reproduced from ref. 34 with permission from Elsevier, copyright 2008); (b) double spinning disc reactor (DSDR) (reproduced from ref. 49 with permission from Elsevier, copyright 2017); and (c) high-speed spinning disk reactor (HSSDR) (reproduced from ref. 178 with permission from the American Chemical Society, copyright 2019).

flow rate and significantly reduce the coefficient of variation, leads to narrower particle size distribution in accordance to residence time distribution (RTD) theory even if it is slightly tends to trigger an increase in the growth rate of nanoparticles.[169,170] These variables are the key factors to determine the optimal flow rate for nanoparticles production.

3.3 Spinning disc reactor

Spinning disc reactor (SDR) is initially developed to enhance heat transfer efficiency on a rotating surface and increase the conversion of a liquid or gas reactions through high gravity fields.[50,172] SDR is a continuous-flow stirred reactor that utilize centrifugal force to exerts thin films on a rotating disc, typically around 50 μm for liquid compounds similar to water.[34] This reactor needs lower energy than other CSTR equipment with higher shear force to increase the mixing rate dan mass transfer frequency.[173] As shown in the scheme of SDR in Fig. 12a, the feed streams is located at the center and radially flows outward affected by centrifugal force of the spinning disc, with high rotating speed usually spanning from 300 rpm to 2000 rpm.[174,175] The shear force implemented at the thin films of reactant provide chemical reaction on the disc surface under specific hydrodynamic condition.[176]

An experiment conducted by Cafiero *et al.* (2002) shows that the reaction of 0.04 M $BaCl_2$ and Na_2SO_4 to create $BaSO_4$ nanoparticles at SDR with supersaturation degree 2000, disc diameter 0.5 m, rotating speed 900 rpm, and reactants flow rate 1.33×10^{-6} m^3 s^{-1} have a larger amount of particles around 3.2×10^9 cm^{-3} compared to T-mixer with number of particles approximately between 2.2×10^8 and 4.0×10^8 cm^{-3}.[173,177] This condition also promotes lower specific dispersed power consumption only around 115 W kg^{-1} and rapid mixing time at 0.9 ms compared to the T-mixer at rotating speed 900 rpm. Similarly, another experiment conducted by Dehkordi and Vafaeimanesh (2009) proves that $BaSO_4$ nanoparticles synthesis reaction in SDR with disc diameter 15 cm and 20 cm and supersaturation level 400–800 undergoes heterogeneous nucleation mechanism, whereas synthesis with supersaturation higher than 800 shows increasement of nucleation rate indicated by sharply declining particle diameter up to 100 nm at supersaturation degree of 2000.[47] The average diameter of nanoparticles obtained from this experiment is relatively higher than those achieved from experiment conducted by Cafiero *et al.*[173] operating at same condition. This could be caused by larger disc diameter that provides more stringent agitation to effectively prevent particles agglomeration. They also proposed that the mixing time of SDR at rotating speed above 750 rpm of 20-cm disk diameter generates smaller particles less than 100 nm at 1000 rpm compared to those achieved from 15-cm disk diameter.

Farahani *et al.* (2017) developed a new SDR design with 20 cm diameter aluminum double spinning disc reactor (DSDR) mounted horizontally in a polycarbonate chamber, as shown in Fig. 12b.[49] This configuration introduces a new variable affecting the conversion results, namely the distance between the disks. This DSDR is designed to be operated at range of 0–4750 rpm. Based on this experiments, it is concluded that DSDR can produces smaller $BaSO_4$ nanoparticles with average diameter 23,4 nm at higher rotating speed (4750 rpm) for both discs, smaller distance between the discs at 0.1 mm, and feed concentration ratio of $BaCl_2 : Na_2SO_4$ equals to 1.3 : 3.1 with flow rate 0.4 L min^{-1}. Meanwhile, nanoparticle with diameter ~60 nm can be achieved at operating rotating speed 500 rpm, lower than conventional SDR.

Recently, a novel modified configuration of a high-speed spinning disk reactor (HSSDR) was proposed as a medium of $BaSO_4$ nanoparticle synthesis reaction.[178] HSSDR model has lower cost and less complex than DSDR. The scheme of HSSDR can be seen in Fig. 12c. The most fine particle size produced from HSSDR is reported to be 16.4 nm with condition operation at rotational disk speed 15 000 rpm, flow rate 450 mL min^{-1}, $BaCl_2$ feed concentration 1.40 mol L^{-1}, Na_2SO_4 feed concentration 3.30 mol L^{-1}, and supersaturation degree at 3362. Similar as the other experiments, the increasing rotational disk speed from 5000 rpm to 15 000 rpm would significantly reduce the particle size from 83.1 nm to 47.6 nm. Additionally, variating the feed entrance radius from 10 mm to 70 mm plays important role in particle size reduction up to 10 nm for both rotating speed 5000 rpm and 15 000 rpm.

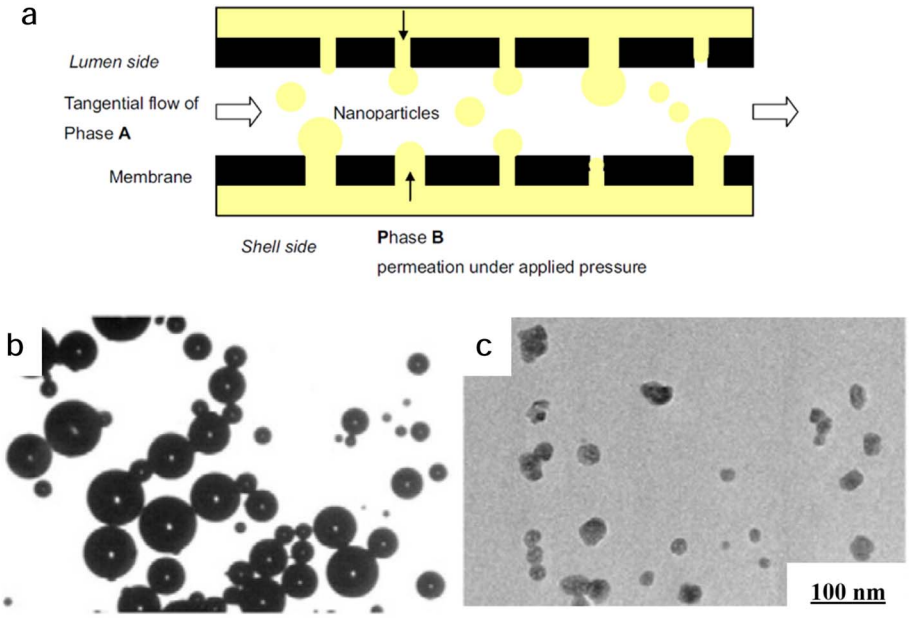

Fig. 13 (a) Scheme of membrane contactor principle process (reproduced from ref. 180 with permission from Global Science Books, copyright 2007); (b) microscope images of microbubbles and (c) TEM images of $BaSO_4$ nanoparticles at $F_G = 300$ mL min^{-1} (reproduced from ref. 187 with permission from Elsevier, copyright 2013).

3.4 Membrane reactor

Many process intensifying reactor technologies have been proposed to enhance nanoparticles synthesis efficiency. However, the particles achieved from these methods still have relatively poor dispersion and difficult to be upscaled to industrial scale of production. Membrane reactor is suggested as an option of nanoparticle synthesis method to obtain more disperse particle. Membrane reactor integrate membrane separation process and the principal of chemical reaction simultaneously.[179] Generally, there are two methods of nanoparticle preparation using membrane reactor, namely the template method and membrane contactor process.[180] The membrane template method is the most common technique to gain nanoparticle conversion in nanotubes, for example gold nanotubes.[181] Membrane contactor process is carried out in two phases, the first phase inserted through the pores while the second phase flows parallel to the membrane surface.[182] Furthermore, the membrane acts as an nonselective interface so the two phases can be separated and in contact simultaneously.[183] Another way to produce nanoparticles with a membrane is in an emulsion system where dispersion occurs in a continuous phase without chemical reactions.[184] Based on research from the past few years, the synthesis of barium sulfate nanoparticles has more frequently been conducted using the membrane contactor process, which involves dispersion in a chemical reaction. The membrane contactor working principle is described in Fig. 13a.

In an experiment conducted by Zhiqian and Zhongzhou (2002), $BaSO_4$ nanoparticles with a diameter of 70 nm were produced using a semi-batch hollow fiber ultrafiltration membrane reactor made from PS, PDC, and PES materials.[51] The driving force, in the form of pressure within the membrane lower than the ambient pressure, was able to increase the nucleation rate of these nanoparticles. Further experiments performed by Jia *et al.* (2003) concluded that the added additives to $BaCl_2$, such as methyl alcohol and ethanol, effective to reduce and control the growth of $BaSO_4$ nanoparticles size to 15 nm due to its higher polarities.[185] Another experiment by Chen *et al.* (2004) using 20% ethyl alcohol in water as a solvent in a nickel membran reactor with both $BaCl_2$ and Na_2SO_4 feed concentration 0.1 M results in particle size reduction from 69.3 nm to 22.6 nm.[186] Du *et al.* (2013) proposed a novel barium sulfate preparation method by dispersion in double membrane reactor with 0.3 MPa nitrogen gas microbubbles injected into the system to improve mixing performance of the synthesis.[187] The microbubbles have an important role to increase the pressure and enhance dispersion within the reactor. Fig. 13b and c show N_2 microbubbles and the final product in this reaction, respectively. The $BaSO_4$ synthesis reaction using nitrogen gas microbubbles which flows at 300 mL min^{-1} with 2.12 mol per L BaS and 0.32 mol per L Na_2SO_4 would produces nanoparticles with a mean size approximately around 40 nm.

Porous hollow fiber membrane is easier to be up-scaled to industrial scale and more compact compared to other micromixer reactor.[188] The conversion rates of membrane reactor can be increased by adding more fibers or using devices in parallel.[189] However, membrane reactors have the potential to experience fouling caused by blockages in the fiber layer due to the crystallization of particles resulting from reactions within the reactor.[190] Moreover, membrane reactor has relatively higher maintenance cost than the other kind of reactors. The summary of precursors, solvents, operating parameters, and

Table 4 Types and condition to obtained $BaSO_4$ nanoparticles at various mean particle size

Reactor	Reactor dimensions	Precursors	Velocity & reaction time	d_{50} (nm)	Ref.
Rotating packed bed (RPB)	—	$BaCl_2$, H_2SO_4 in presence of methanol as solvent and stearic acid (60 °C)	2500 rpm, 18 s	10	48
Rotating packed bed (RPB)	• Inner Diameter: 60 mm • Outer Diameter: 446 mm • Axial Depth: 50 mm • Inlet from inner edge radius: 10 mm • Liq. distributor: • 2 × 10 mm • Nozzles radius: 1 × 2 mm & 4 × 3 mm	$BaCl_2$, Na_2SO_4 in deionized water (25 °C)	800 rpm, typically ~0.1 ms	45	152
T-Mixer	—	$BaCl_2$, H_2SO_4 in pure water	5 mL s^{-1}	70	157
T-Mixer	• Feed tubes diameter: 2 × 0.5 mm • Cross section: 1 mm × 10 mm • Outlet tube length: 3 mm	$BaCl_2$, H_2SO_4 in demineralized water (25 °C)		45	159
T-Mixer	• 2 Reactant inlets (opposite position) and 1 product outlet diameter: 2.4 mm • Mixing channel length: 5 mm	$BaCl_2$, K_2SO_4 in deionized water + dispersing agent (Melpers 0030, polyethercarboxylate)	3.3 m s^{-1}, 0.03 ms	75	162
T-Mixer	• Inlet channel cross-section: 300 × 300 μm^2 • Mixing channel cross-section: 600 × 300 μm^2	$BaCl_2$, H_2SO_4 in demineralized water (25 °C)	100–400 μs	80	164
T-Mixer	• Parallel syringe: 2 × 5 mL • Inlet length: 10 mm • Inlet diameter: 3.4 mm • Mixing arm length: 3 mm, 9 mm, 90 mm • Outlet diameter: 1.9 mm	$Ba(NO_3)_2$, $BaCl_2$, Na_2SO_4, H_2SO_4 in demineralized water (25 °C)	0.5–1.0 ms	1×10^3–1.5×10^3, consists of many fines under 1 μm	177
Modified T-junction – capillary microreactor	• Sprial PTFE microtube inner diameter: 0.8 mm • T-Junction inner diameter: 0.8 mm	BaS black ash, H_2SO_4 in distilled water	0.017–0.27 m s^{-1}; 3.75–15 s	33.8–53.5	32
Y-Mixer	• Inlet tubes diameter: 2 × 0.5 mm • Outlet tube diameter: 2 mm	$BaCl_2$, H_2SO_4 in demineralized water (25 °C)	26 μs	50	72
Spinning Disc Reactor (SDR)	• Feed inlet radius: 50 mm • Disc diameter: 50 cm	$BaCl_2$, Na_2SO_4 in demineralized water (25 °C)	900 rpm; 0.90 ms	700	173
Spinning Disc Reactor (SDR)	• Feed inlet radius: 50 mm • Disc diameter: 15–20 cm • Inlet tubes length: 10 cm • Inlet tubes diameter: 2 × 3 mm • Inlet tubes distance: 2 × 5 mm • Tubes-disc distance: 10 mm	$BaCl_2$, Na_2SO_4 in demineralized water (25 °C)	1500 rpm; 1.25 ms	38	47
Double coaxial spinning disc reactor (DSDR)	• Feed inlet radius: 70 mm • Inlet nozzle: 1 mm for $BaCl_2$ solution and 2 mm for Na_2SO_4 solution • Disc diameter: 2 × 20 cm • Discs distance: 0.1 mm • Discs diameter: 20 cm	$BaCl_2$, Na_2SO_4 in demineralized water (25 °C)	±4750 rpm; <0.5 ms 15 000 rpm; 0.93–2.88 ms	23.4 16.4	49 178

Table 4 (*Contd.*)

Reactor	Reactor dimensions	Precursors	Velocity & reaction time	d_{50} (nm)	Ref.
High-Speed Spinning Disc Reactor (HSSDR)	• Discs distance: 5 cm • Feed nozzle diameter: 2 × 5 mm • Nozzles distance: 4–140 mm • Nozzles-disc distance: 5 mm • Feed entrance radius: 70 mm	$BaCl_2$, Na_2SO_4 in demineralized water (25 °C)			
Membrane reactor	• Inner diameter: 1 mm • MWCO: PES/PDC (1000 Da) PS/PDC (30 000 Da) • Membrane length: 13 cm	$BaCl_2$, Na_2SO_4 in demineralized water (25 °C)	0.589 m s^{-1}, 480 min	70	51
	• UF membrane: Inner diameter: 10 mm Effective length: 13 cm PS/PDC (30 000 Da)	BaS, Na_2SO_4 in presence of methyl alcohol	0.92 m s^{-1}	15	185
	• Microfiltration membranes: 5 μm stainless steel 0.9 μm Ni 0.2 μm Ni • Active membrane area: 12.5 mm^2	$BaCl_2$, Na_2SO_4 in presence of ethyl alcohol	22–24 mL min^{-1}	20	186
N_2 microbubbles-aided membrane reactor	• 5 μm stainless steel membrane • Average pore size: 0.5 μm • Active membrane area: 12, 5 mm^2 • Porosity: 65% • Main channel dimension: 20 mm × 2 mm × 0.5 mm	BaS, Na_2SO_4	120 mL min^{-1}, 2.4 ms	40	187

dimension of reactors used in $BaSO_4$ nanoparticles synthesis are provided in Table 4.

4. Barium sulfate nanoparticle application in various industries

4.1 Medical applications of barium sulfate nanoparticles

Recently, researchers are developing novel nanoparticle and nanocomposite materials for the advancement of the medical industry. Barium sulfate nanoparticles have garnered significant interest from researchers in the medical sector because of their distinctive properties, such as inertness, high dispersion rate, substantial X-ray attenuation, insolubility, biocompatibility, and colloidal stability in aqueous solutions.[191,192] Hence, $BaSO_4$ nanoparticles have since investigated as superior material to increase accuracy of medical imaging technique, mainly as X-ray contrast agent. Furthermore, X-ray shielding material is also needed to minimize the exposure of ionizing radiation to human cells. Some barium sulfate based nanocomposite have been proposed as a non-toxic X-ray shielding material, replacing lead based material which is toxic and highly hazardous to the ecological system.[193]

Meagher *et al.* (2013)[41] synthesized 40 nm monodisperse $BaSO_4$ nanoparticles in water-in-oil emulsion system, which encapsulated by dextran as a stabilizer.[16] This synthesis mechanism produces well-dispersed in water $BaSO_4$ nanoparticles with high X-ray attenuation (100–200 Hounsfield Unit (HU)) compared to soft tissues (20–80 HU). Larsson *et al.* (2015) optimized an imaging technique using $BaSO_4$ and gadolinium as a dual-modality contrast agent component for detecting and monitoring diseases.[194] This method involves macrophages combined with gadolinium and barium sulfate nanoparticles. Specifically, mouse alveolar macrophages are loaded with $BaSO_4$–Gd at a ratio of 2 : 4 million cells to serve as a contrast agent in X-ray and magnetic resonance imaging (MRI). Lopresti *et al.* (2020) investigating a novel epoxy resins composite with barium sulfate as a supplementary substance for X-ray shielding purposes. This composite is coated by 0.75 grams stearic acid to reduce sedimentation and increase its dispersibility.[195] Another nanocomposite designed by Abdolahzadeh *et al.* (2023) for X-ray shielding consists of polyethylene, tungsten oxide, bismuth trioxide, barium sulfate, and graphene oxide, as shown in Fig. 14a.[196] The optimal composition to gains the maximum thermal resistance of the X-ray shield is achieved at 90%-wt HDPE and 10%-wt $BaSO_4$–GO. This nanocomposite has a higher melting point of 132.1 °C while maintaining its crystallinity at 60.1%. Furthermore, the addition of 25%-wt WO_3/Bi_2O_3/GO has a transmission factor of 10% at 50 kVp with 6 mm thickness, aligns with the compatibility standards of Pb-based protective apron with thickness of 5.5 mm while reducing its mass to 4.10 times lighter than Pb-based apron.

Further experiment conducted by Kilian *et al.* (2023) developed a dual-modality contrast agent consists of barium sulfate and cyanine tetrafluoroborate salt pigments for both X-ray and photoacoustic imaging (PAI) in gastrointestinal tract.[197] Result shows that combination of 40%-w/v barium sulfate and 5 mg per mL pigment can be used as contrast agent of Nd–YAG nonablative laser at a wavelength of 1064 nm, which has been widely used in PAI and relatively safe for on skin treatment.[198] Meanwhile, Tokonami *et al.* (2024) modifies $BaSO_4$ nanoparticles properties by coating them with multiwalled carbon nanotubes (MWCNTs) to increase the interfacial bonds and tensile modulus.[199] Multiwall carbon nanotubes consist of multiple layers of graphite sheets rolled into a cylindrical shape, with an interlayer spacing of 3.4 Å and mainly synthesized through chemical vapor deposition (CVD) route.[200,201] PS is considered to be used for matrix formation of $BaSO_4$–MWCNTs nanocomposite due to its solubility in organic solvent.[202] The PS/$BaSO_4$–MWCNTs composite, as shown in Fig. 14b, does not exhibit fracture traces at the interface, indicating that cohesive failure occurs as a result of stress concentration within the matrix. This observation suggests that the PS resin bonds with the MWCNT structure through π-bond opening on the $BaSO_4$ surface,[203] thereby reduces interfacial slip between the PS and $BaSO_4$ components.[204] The modification of $BaSO_4$ nanoparticles was proven did not disrupt the X-ray attenuation.

Aside from its main usage as contrast agent, $BaSO_4$ nanoparticles also have been proposed to improve orthopedic advancement, *i.e.* analysis of bone structure and bone cement filler. Leng *et al.* (2005) suggested barium sulfate nanoparticles

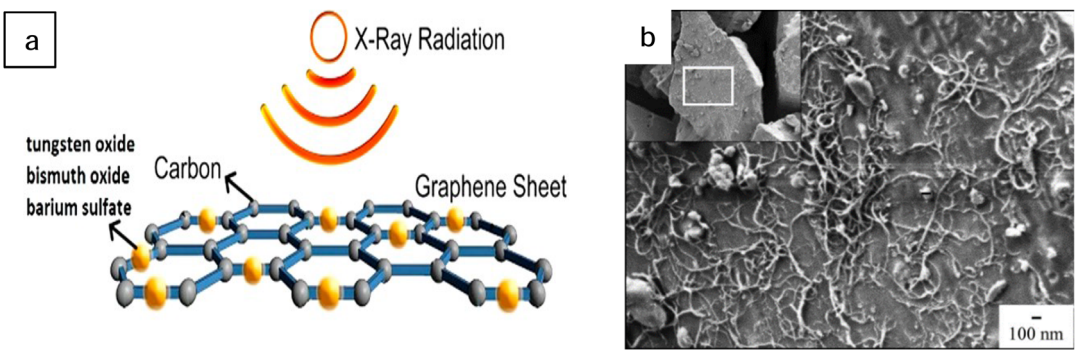

Fig. 14 (a) Nanocomposite structure on nanographene oxide sheets for X-ray shielding (reproduced from ref. 196 with permission from International Journal of Radiation Research, copyright 2023); (b) SEM images of MWCNT-coated $BaSO_4$ surface (reproduced from ref. 199 with permission from Wiley, copyright 2024).

as contrast agent of micro-computed tomography (μCT) for bone microstructure analysis.[205] Microdamage on the bone structure is an condition arising from continuous fatigue or overloading.[206] Generally, there are two types of microdamages, namely linear microcracks and diffuse damage.[207] The most common microdamage is linear microcracks with length around 30–100 μm.[208] In that case, μCT scan with $BaSO_4$ as contrast agent is one of the most prominent solution to locate the bone microcracks before determine further treatment.

Leng *et al.* (2005) prepared $BaSO_4$ nanopowder with 1 M $BaCl_2$ and 0.1 M Na_2SO_4, resulting an average particle size approximately 50 nm.[205] The particles were injected into cortical bone tissue and coated the inner walls of the holes, resulting in a deposited thickness of $BaSO_4$ nanoparticles which are smaller than the hole diameter. The measured hole diameter and volume with deposited nanoparticles appeared larger than its actual size and volume, indicating an approximately eightfold discrepancy in volume measurement. Further evaluation done by Leng *et al.* (2008) regarding to their previous experiment proves that the use of barium sulfate contrast agent allows for the imaging of microdamage without destroying the specimens, enabling repeated measurements and studies.[209] The relative volume of the stained region, indicative of microdamage accumulation, was found to be amplified with an increasing number of loading cycles in accordance to the power law.[210]

Fang *et al.* (2014) modified $BaSO_4$ nanoparticle synthesis to be implemented in bone cements by using 0.25 M $K_2S_2O_8$ with 50 mL of 0.5 M KOH, $BaCl_2$, and difunctional surface modification agent of (2-(methacryloyloxy) ethyl dimethyl-(3-sulfopropyl)) ammonium hydroxide (MSAH) with MSAH/$BaCl_2$ molar ratio ranging from 0 to 0.128.[211] The produced 10–30 nm spherical $BaSO_4$ nanoparticles integrated with polymethyl methacrylate (PMMA) matrix to strengthen the bone cements. MSAH-functionalized $BaSO_4$ nanoparticles effectively improved the bending modulus of the bone cement from 2293 MPa to 3100 MPa while the compressive strength gradually increased from 96 MPa to 132 MPa due to the increased MSAH coating and decreased particle size. The increment of the MSAH-functionalized $BaSO_4$ nanoparticles to 20%-wt would result in the improvement of radiopacity and did not affect the biocompatibility of the bone cements.

Barium sulfate nanoparticles modification method also have been through some advancement for cancer treatment. Nowadays, several methods have been proposed to cure cancer and tumors, such as stem cells for lymphoma treatment, immune-stimulating vaccines for renal cell cancer (RCC), radiofrequency ablation for liver metastasis, and nanoparticle-based drug delivery system.[212–215] Targeted alpha therapy utilized nanoparticles to deliver radionuclide which would emits alpha particles to treat the targeted tumor cells.[216] Targeted alpha therapy have shorter route which establish higher linear energy transfer (LET) and relative biological effectiveness (RBE).[217,218] Targeted alpha therapy is considerably less toxic compared to other kind of radiation methods. Hence, it garnered more interest in the development of cancer treatment technologies.

Reissig *et al.* (2019) developed a novel one-pot approach for the synthesis of barium sulfate nanoparticles as a carrier to bond Ra with the targeted molecule.[219] This new route is designed to accommodate targeted alpha therapy. The carriers were built by the addition of 6.6 mg $(NH_4)_2SO_4$ feeding solution to 61 mg $BaCl_2$ and 46 mg alendronate stock solution under stirring at 1000 rpm and with Ba^{2+}/SO_4^{2-} ratio of 6 : 1. This precipitation produces barium sulfate nanoparticles with a mean diameter of 140 ± 50 nm. Alendronate serves as a binding agent between $BaSO_4$ nanoparticles and the target molecule, featuring a phosphonate group and a peptide linkage.[220] These synthesized alendronate-containing $^{[133Ba]}BaSO_4$ and $^{[224Ra]}BaSO_4$ nanoparticles exhibited a very low activity release of less than 5%, $BaSO_4$ nanoparticles exhibited a very low activity release of less than 5% and their reactivity are confirmed by the result of active ester coupling, which are favoured for theragnostic purposes. However, this method only has an binding efficiency of 20% ^{224}Ra with the $BaSO_4$ nanoparticles. This discovery became the basis for further research conducted by Reissig *et al.* (2020), which involved a two-step precipitation method to produce $BaSO_4$ nanoparticles with smaller size around 9.1 nm and more homogenous spherical orthorhombic geometry.[221] These $BaSO_4$ nanoparticles act as carriers for radium, barium, lutetium, indium, and zirconium with high radionuclide retention (>90%) and higher ^{224}Ra radiochemical yields of 31%.

Aside from targeted alpha therapy, transcatheter arterial embolization is also considered as an alternative to cancer medication. Transcatheter arterial embolization (TAE) can be defined as a non-invasive therapy by inserting a catheter into a blood artery, commonly employed to remedy unresectable and neuroendocrine tumors, and liver cancer.[222–224] However, the lack of inherent radiopacity in conventional embolic materials limits the real-time tracking and precise positioning of these agents, leading to challenges in controlled delivery and efficacy assessment. Wang *et al.* (2015) introduces a novel embolic agent consisting of barium alginate (ALG) microspheres loaded with *in situ* synthesized $BaSO_4$ nanoparticles, prepared *via* a one-step droplet microfluidic technique combined with external ion-crosslinking.[225] The $BaSO_4$/ALG microspheres is more durable and have excellent X-ray visibility and embolic efficacy compared to the commercially available calcium alginate microspheres, as confirmed by *in vitro* and *in vivo* assays. The addition of 5–9 wt% $BaSO_4$ nanoparticles in this admixture improve the thermal resistance below 220 °C and also proven to enhance the visibility under X-ray up to 14 days.

Another tumor theragnostic supporting material is developed by Shukla *et al.* (2023) using carrageenan-linked $BaSO_4$ nanoparticles.[226] The 200–300 nm Ba-linked iota carrageenan have better fluorescence activity than the powered Ba-carrageenan. The cancer cell selectivity observed through the escalation of pK_a while some Ba^{2+} ions released in acidic environment. This ionization mechanism would disrupt cells homeostasis, consequently trigger the lysis of the cancer cells. Meanwhile, investigation on the cytotoxicity of the $BaSO_4$ nanoparticles synthesized *via* one-step hydrothermal method shows viability decreasement of the cancer cell implanted in a mouse at a dose of 823.8 μg mL^{-1}.[227]

4.2 Barium sulfate nanoparticles application in polymer industry

In recent years, the incorporation of barium sulfate nanoparticles into the polymer industry has sparked major interest due to their exceptional properties and versatile applications. $BaSO_4$ nanoparticles have abundant advantages to improve polymers' characteristics, including high density, chemical inertness, thermal resistance, and unique optical properties.[228] Consequently, barium sulfate nanoparticles have garnered significant attention from researchers and manufacturers to escalate the performance and functionality of polymer-based products. Furthermore, increasing consumption of polymer-based fibers for textile industry and coating materials also plays a role in high demand of better polymer products.

Chen *et al.* (2009) analyze the modification of high density polyethylene (HDPE) with $BaSO_4$ nanoparticles as an additive, especially in terms of its mechanical properties for anti-wave applications in marine environments.[229] 40 nm $BaSO_4$ nanoparticles and sodium stearate were mixed to provide organic functional bonds on their surface before melded with HDPE at 210 °C to produce $BaSO_4$/HDPE nanocomposite. Sodium stearate alter the interstitial particle spaces to ensure better dispersion of barium sulfate so it have strong adhesion with the polymer matrix.[230,231] From this experiment, it is concluded that the addition of $BaSO_4$ nanoparticles should be at the maximum amount of 2%-wt due to lower interface binding strength caused by excess doping material in the polymer matrix structure. The differences in the bond strength between the nanocomposites at varying concentrations can be seen visually from SEM images in Fig. 15a–d. Increment of half crystallization time and peak crystallization temperature was observed with the addition of $BaSO_4$ content. The highest half crystallization time at 0.55 min and peak crystallization temperature at 114.1 °C was achieved by 5%-wt $BaSO_4$ nanoparticles addition into the nanocomposite. This phenomena happened due to unstable state caused by faster heterogenous nucleation rate and crystallization rate of the nanocomposite, identified by its narrow peak and smaller supercooling degree at 11 °C.[232,233] However, further aggregation of $BaSO_4$ nanoparticles above 1%-wt would defects and reduce the toughening effect of the product. Additionally, the tensile yield stress of HDPE/$BaSO_4$ nanocomposites is mainly affected by the interface stress transfer. This interfacial binding is also increase 10.4% storage modulus for 5%-wt $BaSO_4$ nanoparticles at 25 °C. Thus, the optimal mechanical properties for anti-wave material is achieved by addition of 1.0 wt% $BaSO_4$ nanoparticles which reached the highest impact strength of 63.6 kJ m^{-2} compared to pure HDPE impact strength which is around 8.5–9.34 kJ m^{-2},[234,235] as in this case impact strength is a critical factor for materials to withstand fractures when subjected to stress from wave forces.[236]

Another experiment conducted by Li *et al.* (2012) to make $BaSO_4$/polypropylene (PP) nanocomposite using similar method from Chen *et al.* (2009) with dodecyl benzene sulfonic acid (DBSA) as compatibilizer agent.[229,237] DBSA was chosen due to its non-hygroscopic anionic properties and its chemical structure which consists of long dodecyl chain attached to a benzene ring and hydrophilic sulfonic group that would create protective layer and stabilize the particles by the steric hindrance.[238] The presence of $BaSO_4$ nanoparticles inversely affects materials' consistency at various temperature compared to the flow index, suggesting that these nanoparticles create strong bonds with polymers, thereby impeding the slippage among polymer molecules.[239,240] Therefore, the $BaSO_4$ content must be adjusted

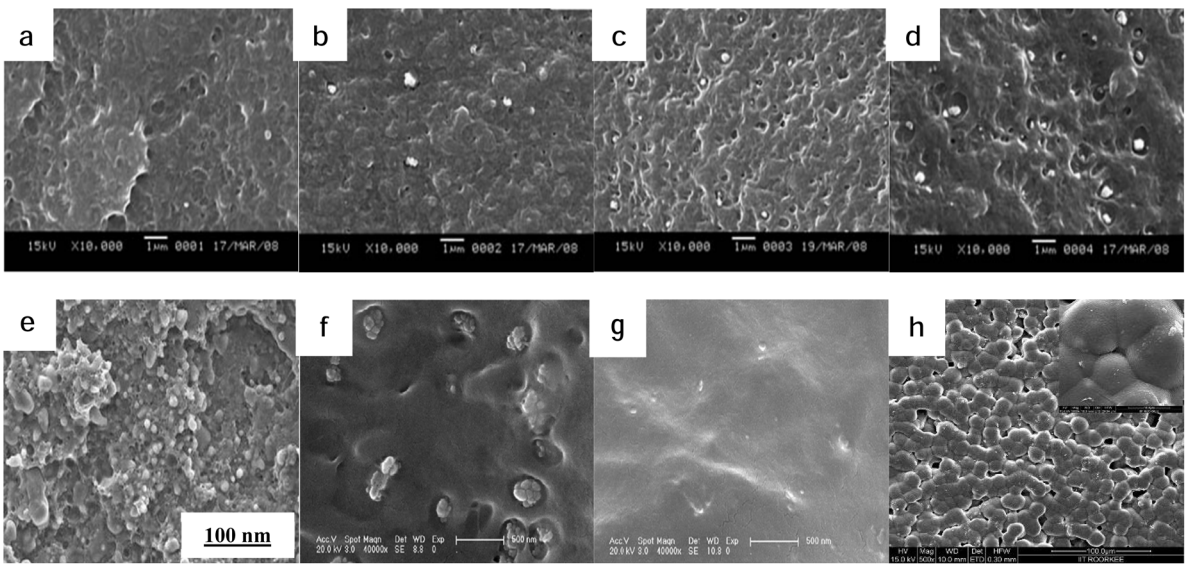

Fig. 15 SEM micrographs of HDPE nanocomposites at various $BaSO_4$ content: (a) 0%-wt; (b) 1%-wt; (c) 2%-wt; and (d) 4%-wt (reproduced from ref. 229 with permission from SAGE Publications, copyright 2009); (e) SEM image of $BaSO_4$/PP nanocomposite fibers (reproduced from ref. 237 with permission from World Scientific, copyright 2012); (f) SEM images of 2%-wt blank $BaSO_4$/PET and (g) 2%-wt modified $BaSO_4$/PET nanocomposites (reproduced from ref. 242 with permission from Elsevier, copyright 2011); (h) SEM image of PVDF/$BaSO_4$/nanoclay with mixing concentration/gram ratio of 5 : 0.68 : 0.10 (reproduced from ref. 247 with permission from Springer, copyright 2017).

in terms of shear thinning to maintain the mobility of the PP molecules to facilitate spinning to form fibres. The effectiveness of interface interaction is proven to escalate the mechanical properties of the $BaSO_4$/PP fibers. Enhancing the draw ratio of fibers leads to an improved preferential orientation along the fiber chain axis.[241] This tendency makes the storage modulus of fibers increase at a higher amount of 60 wt% $BaSO_4$. Thermogravimetry analysis of the $BaSO_4$/PP hybrid fibers shows an escalation of the onset of degradation temperatures from nanocomposite fibers with 40%-wt and 60%-wt of $BaSO_4$, approximately 10–20 °C higher than the pure PP fiber. The SEM image of $BaSO_4$/PP nanocomposite fibers is presented in Fig. 15e.

Similar experiment was conducted by Gao *et al.* (2011) with precipitation method using stearic acid as hydrophobic agent to support the formation of 100–150 nm elliptical $BaSO_4$ nanoparticles before combined with poly (ethylene terephthalate) to create $BaSO_4$/PET nanocomposites.[242] TGA data between pure PET and 2%-wt modified $BaSO_4$/PET shows increasing decomposition temperature at 445.18 °C. This condition indicates that the integration of $BaSO_4$ into the PET matrix results in increased thermal decomposition temperatures, thereby gave better thermal stability of PET. On the other hand, excessive agglomeration of doped $BaSO_4$ would reduce thermal stability of this nanocomposite due to the weakened chains in polymer matrix and localized overheating. The final product with well-dispersed molecules and the best mechanical properties is obtained by 2%-wt modified $BaSO_4$/PET nanocomposites at supercooling degree of 16.36 °C. SEM images of blank and modified 2%-wt $BaSO_4$/PET nanocomposites which are respectively presented in Fig. 15f and g support the above statement. The same group then proceeded to do further research to analyze the thermal stability and crystallization tendency by using *in situ* polymerization of TPA, EG, and $BaSO_4$ nanoparticles modified with stearic acid.[243] TGA data revealed that $BaSO_4$/PET nanocomposites maintain excellent thermal stability by showing no substantial mass loss below 360 °C. Based on Friedman method calculation, the activation energy for thermal decomposition of nanocomposites is higher compared to pure PET sample. Thus, the inclusion of $BaSO_4$ nanoparticles hinders char formation and prevents the escape of volatile byproducts during thermal decomposition.

Kulkarni *et al.* (2013) proposed a novel approach with *in situ* synthesis method of poly(styrene–butylacrylate–acrylic acid) latex/$BaSO_4$ nanocomposite.[244] 40 nm $BaSO_4$ nanoparticles were produced *via* micellar solution spray process and sonicated with SDS and sorbitan monolaurate before stirred at 70 °C to combine them with styrene, butyl acrylate and acrylic acid monomers to create the desired nanocomposite. This method ensured a homogeneous dispersion of the nanoparticles within the latex matrix, as shown on the TEM images of $BaSO_4$ nanoparticles. Atomic Force Microscopy (AFM) images confirmed that the uniform dispersion of $BaSO_4$ nanoparticles must be at the maximum loadings of 2%-wt $BaSO_4$ to avoid excessive agglomerates. Maximum tensile strength and elongation at break were achieved at a $BaSO_4$ loading of 1.5%-wt, with values reaching 7.9 MPa and 387%, respectively. The enhancement in mechanical properties is attributed to the strong interfacial adhesion between the $BaSO_4$ nanoparticles and the PSBA latex matrix. Incorporation of 2%-wt $BaSO_4$ nanoparticles sets the onset and endset decomposition temperature at the higher value of 392 °C and 456 °C respectively, indicating improved thermal stability of this nanocomposite. The $BaSO_4$ nanoparticles in this composite film also notably lower water absorbance percentage from 25% to approximately 5% in 72 hours, demonstrating their superior ability to enhance moisture resistance compared to the pure PSBA latex film. Therefore, this composite is has the potential to improve the quality of PBSA latex for various coating applications.

Another synthesis route for barium sulfate nanoparticles to modify acetal resin using a thermoplastic injection system is proposed by Ahmed and Hasan (2017).[245] The mean force required to cause failure decreased from 12.551 kN for the control sample to 10.096 kN for the modified $BaSO_4$/acetal nanocomposite. The agglomeration of $BaSO_4$ nanoparticles would break the binding interface of the polymer matrix, resulting in a slight reduction in nanocomposite material strength. The optimal amount of $BaSO_4$ nanoparticles required for acetal resin doping material to maintain its radio-opacity properties is 3%-wt. This nanocomposite has radio-opacity equivalent to 2 mm thickness of aluminum without significantly altering the color or flexibility of the acetal resin while ensuring adequate radio-opacity for dental applications. A similar approach was explored by Romero-Ibarra *et al.* (2012), who successfully produced nanocomposites consisting of 1%-wt of $BaSO_4$ nanoparticles and polyurethane using a melt extrusion technique.[246] This composite is less brittle than the other one containing 40%-wt of $BaSO_4$. The $BaSO_4$/PU nanocomposite shows potential for biomedical tracking of microplastics inside the human body. In a related study, Li *et al.* (2022) successfully modified a thermoplastic polybutylene terephthalate (PBT)/polyethylene terephthalate (PET) composite by incorporating $BaSO_4$ nanoparticles to enhance heat resistance and impact tolerance.[15] The surface of $BaSO_4$ nanoparticles were adjusted with aluminate before being added to the blend. The optimal composition of the PBT/PET/$BaSO_4$ composite was found to be PBT : PET at 90 : 10%-wt with 4%-wt of $BaSO_4$ nanoparticles. This formulation increased the heat distortion temperature to 174.4 °C, 22.6% higher than pure PBT/PET, and enhanced tensile strength to 59.72 MPa, 11.6% higher compared to unmodified PBT/PET blend.

Aside from their leverages in terms of thermal stability and opaqueness, $BaSO_4$ nanoparticles also considered as a potential material to construct UV-Vis absorbing feature in polymer. Agarwal *et al.* (2017) developed PVDF nanocomposites with alkyl quaternary ammonium bentonite montmorillonite nanoclay (MMT) and $BaSO_4$ nanoparticles, showcasing its improved thermal stability and UV-shielding properties.[247] 25–33 nm $BaSO_4$ nanoparticles were synthesized using an *in situ* deposition method with polyethylene glycol (PEG) as stabilizer surfactant. Then, $BaSO_4$ nanoparticles were mixed with PVDF and nanoclay in DMSO solvent to produce nanocomposite which can be seen in Fig. 15h. TGA data shows that this nanocomposite has higher decomposition temperature >600 °

Table 5 Applications of $BaSO_4$ Nanoparticles

Application	Nanocomposites	Special features	Ref.
Medication	$BaSO_4$ nanoparticles stabilized with dextran	High X-ray attenuation (100–200 HU), well-dispersed in water	16
	$BaSO_4$–Gd contrast agent	Dual-modality contrast for X-ray and MRI	194
	Epoxy resin composite with $BaSO_4$ NP and stearic acid	Improved X-ray shielding, reduced sedimentation	195
	HDPE–$BaSO_4$–GO nanocomposite	X-ray shielding, high thermal resistance, lightweight alternative to Pb-based aprons	196
	$BaSO_4$ with cyanine tetrafluoroborate salt pigments	Dual-modality contrast agent for X-ray and PAI (photoacoustic imaging)	197
	PS/$BaSO_4$–MWCNTs composite	Increased interfacial bond strength, improved tensile modulus, and cohesive failure prevention without disrupting X-ray attenuation	199
	$BaSO_4$ nanoparticles for μCT imaging	Accurate bone microcracks locations detection, improved microdamage visualization	205 and 209
	MSAH-functionalized $BaSO_4$–PMMA composite	Strengthened bone cements, improved bending modulus and compressive strength, increased radiopacity	211
	Radium-binded $BaSO_4$ nanoparticles	Targeted alpha therapy for cancer treatment, high radionuclide retention (>90%)	219 and 221
	$BaSO_4$/ALG microspheres	Enhanced X-ray visibility up to 14 days, improved embolic efficacy for TAE (transcatheter arterial embolization)	225
	Carrageenan-linked $BaSO_4$ nanoparticles	Fluorescence activity, cancer cell selectivity *via* pK_a escalation	226
	Hydrothermally synthesized $BaSO_4$ nanoparticles	High cytotoxicity for cancer cell elimination	227
Polymer	$BaSO_4$/HDPE	Enhanced mechanical properties for anti-wave applications; optimal impact strength at 1%-wt $BaSO_4$; increased crystallization temperature and modulus at 5%-wt $BaSO_4$	229
	$BaSO_4$/PP	Increased fiber orientation; onset of degradation temperature increased by 10–20 °C	237
	$BaSO_4$/PET	Increased thermal stability and decomposition temperature at 2%-wt $BaSO_4$	242
	TPA/EG/$BaSO_4$	Increased thermal stability and reduced thermal weight loss	243
	$BaSO_4$/PSBA latex	Improved dispersion, tensile strength, and elongation at break; enhanced thermal stability; reduced water absorbance (from 25% to ∼5%)	244
	$BaSO_4$/acetal resin	Maintains radio-opacity equivalent to 2 mm aluminum; optimal doping at 3%-wt without altering color or flexibility	245
	$BaSO_4$/PU	Less brittle than low $BaSO_4$ content composites; potential for biomedical tracking applications	246
	$BaSO_4$/PBT-PET	Enhanced heat resistance (+22.6%) and tensile strength (+11.6%)	15
	$BaSO_4$/PVDF/MMT	Improved thermal stability (>600 °C); enhanced UV-Vis absorbance	247
	$BaSO_4$/PVA	Maximum UV-Vis absorption at 600 nm achieved at 2 wt% $BaSO_4$	250
	$BaSO_4$/epoxy resin	High solar reflectance; radiative cooling effect; increased tensile strength (+16.6%)	251

C, whereas the average primary decomposition temperature of pure PVDF is ranging from 400–510 °C.[248] The exothermic melting peak at 160–170 °C is caused by presence of MMT which act as heterogeneous nucleating agent, hence it is lower than the pure PVDF melting point at 174.8 °C.[249] The UV-Vis spectroscopy data revealed that UV-Vis absorbance is mainly influenced by $BaSO_4$ content, which escalated from 20% to 60% when the $BaSO_4$ is increased twofolds. Moreover, the optimal mixing concentration/gram ratio of PVDF/$BaSO_4$/Nanoclay to obtain the most effective UV-Vis absorbing composite material is 5 : 0.68 : 0.10. Further study conducted by Ahmad *et al.* (2021) investigated the effects of barium sulfate addition in polyvinyl acetate (PVA), especially their UV-Vis absorbance properties.[250] From this experiment it is concluded that the maximum UV-Vis light absorption at a wavelength of 600 nm can be achieved by adding 2%-wt of $BaSO_4$ to create the PVA/$BaSO_4$ nanocomposite.

In addition to its utilization in polymer structure as a UV-Vis absorber, $BaSO_4$ nanoparticles with high dispersibility have also been proposed as an environmentally friendly alternative for cooling systems. Wu *et al.* (2023) designed a $BaSO_4$–epoxy resin composite film with radiative cooling feature.[251] This composite

constructed of spherical $BaSO_4$ clusters formed using directly precipitated PVP-modified $BaSO_4$ nanoparticles as their template. The obtained $BaSO_4$–epoxy resin composite demonstrated a solar reflectance of 71% and the ability to cool down the temperature up to 13.5 °C with excellent amount of tensile strength, which is 16.6% higher than conventional radiative cooling films. All of these innovative applications of $BaSO_4$ nanoparticles are summarized in Table 5.

5. Green synthesis of $BaSO_4$ nanoparticles

New approaches to the green synthesis of nanomaterials are currently receiving a great deal of attention in the field of nanomaterial engineering.[252] Many studies have developed the synthesis process of barium sulfate nanoparticles, for example *via* chemical precipitation, hydrothermal, and solution combustion.[50,227,253] However, these methods have generated new problems in environmental pollution due to hazardous and toxic waste. Therefore, researchers are focusing on solutions to find nanomaterials synthesizing method that can optimize industrial processes and medical benefits to make them more sustainable and environmentally friendly. One of the most prominent routes to environmentally friendly nano-sized products is through green synthesis using plant extracts. This approach fosters the development of less toxic nanomaterials and reduces production costs.

Chen *et al.* (2016) investigated the characteristics of barium sulfate nanoparticles obtained from precipitation with soluble biomolecules from fruit extracts.[254] Fig. 16a and b show that $BaSO_4$ synthesis without fruit extract would produces larger final products which are more difficult to disperse. The initial nanoparticles obtained with kiwifruit extracts is found in leaf-shaped crystals with toothed edge, as revealed in Fig. 16c and d, while $BaSO_4$ nanoparticles with 2–4 μm thorn spherical were gained in tomato extract, which is validated by SEM images in Fig. 16e and f. Fig. 16g and h show that rod-shaped or quasi-spherical $BaSO_4$ crystals, ranging from a few hundred nanometers to a few micrometers can be produced in addition of orange juice. In contrast, carrot juice yielded quasi-spherical $BaSO_4$ nanocrystals, as shown in Fig. 16i and j. Thus, carrot extract has the most potential to inhibit crystal growth. This synthesis mechanism involves aggregate formation by binding Ba^{2+} ions with biomolecules, which then adsorbed onto $BaSO_4$

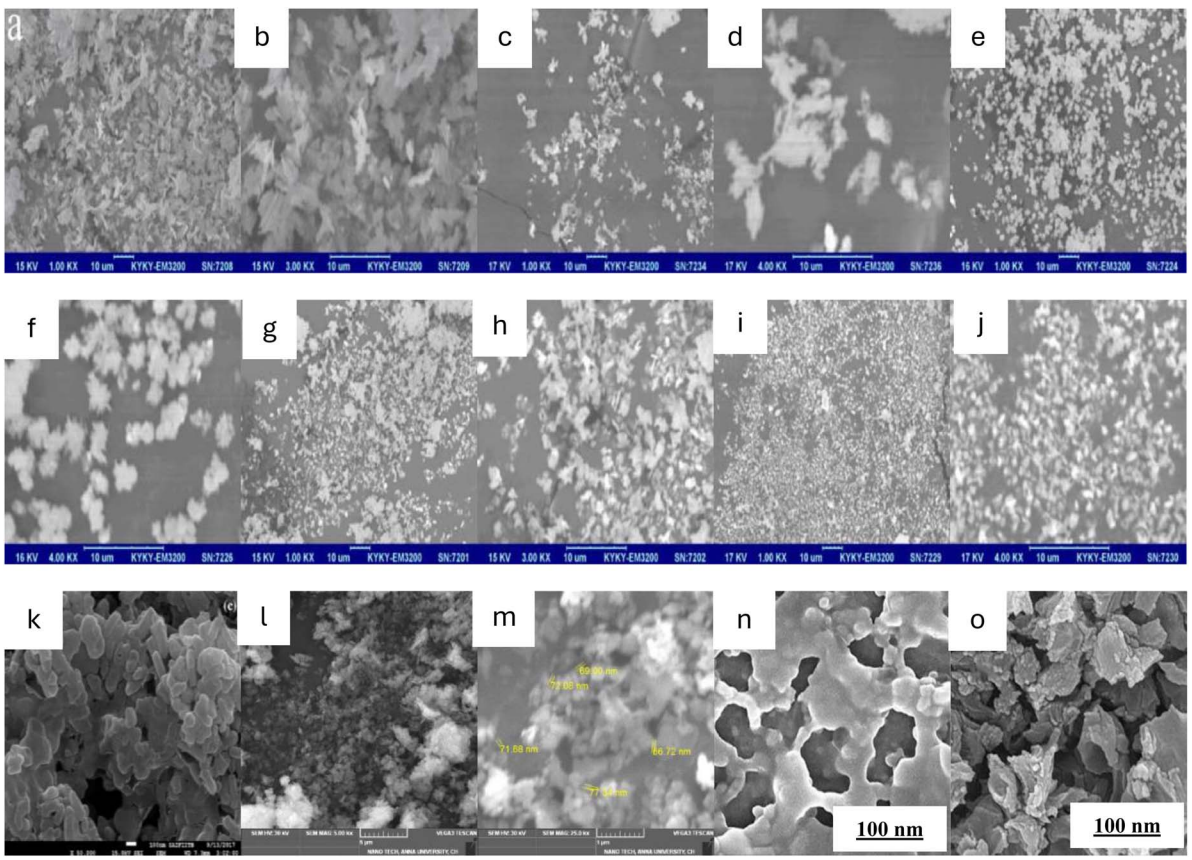

Fig. 16 SEM images of $BaSO_4$ as final product: (a and b) without any extracts; (c and d) with kiwifruit extracts; (e and f) with tomato extracts; (g and h) with orange extracts; (i and j) with carrot extracts (reproduced from ref. 254 with permission from EDP Sciences, copyright 2016); (k) FEG-SEM of $BaSO_4$ nanoparticles synthesized using *Azadirachta indica* under magnification 100 nm (reproduced from ref. 38 with permission from Springer, copyright 2019); (l) and (m) SEM images of $BaSO_4$ nanorods synthesized using *Azadirachta indica* (reproduced from ref. 265 with permission from Environmental Nanotechnology Society, copyright 2024); FESEM analysis of $BaSO_4$ nanoparticles at pH = 7 in presence of (n) starch and (o) PAC (reproduced from ref. 276 with permission from Islamic Azad University, copyright 2019).

crystal surfaces gained from nucleation, and subsequently dictating the structure of the final products.[255–258]

Another experiment conducted by Jha *et al.* (2019) investigated a new method ultrasonic-assisted green synthesis of $BaSO_4$ nanoparticle synthesis by using neem (*Azadirachta indica*) leaf extract.[38] Neem leaf extracts consists of many phytocomponents, such as azadirachtin, nimbin, margosin, and several types of flavonoid, that can be utilized as nucleating agent and growth modifying agent in the main reaction of nanoparticle synthesis.[259–262] Agglomeration reduced by tuning the ultrasonication mixing which consequently would increase the temperature in reaction system and nucleation rate.[263,264] The average crystalline size of barium sulfate nanoparticles obtained from this experiment with 0.05 M $BaCl_2$ and 0.05 M Na_2SO_4 is ~55.6 nm, as presented in Fig. 16k. These $BaSO_4$ nanorods have high thermal stability up to 310 °C with weight loss only around 7.69%. Further experiment using neem leaves extract by Saravanan *et al.* (2024) involves similar co-precipitation method with the same reactants as previous attempt by Jha *et al.*[38,265] Instead of incubating the precipitate at 37 °C for 24 hours before centrifugated, Saravanan *et al.* drying the obtained $BaSO_4$ particles in a hot-air oven at 100 °C for 2 hours. As shown in Fig. 16l and m, $BaSO_4$ nanoparticles product from this experiment have a mean particle size of 71.34 nm with rod-like shape.

Aside from plant extracts, several compounds can also be considered as an alternative to enable green synthesis route for nanoparticles synthesis. For example, glycerol is a hydrophilic organic triol compound, usually found as a byproduct of lipid hydrolysis.[266–268] This compound is biodegradable, non-toxic, and cheaper than other available reducing agents.[269,270] Hosseini *et al.* (2019) developed a novel auxiliary solution consists of 5 mL pure glycerol, 3 mL concentrated HCl, 1 mL isopropanol, 4 grams NaCl, and 30 mL deionized water to stabilize barium sulfate nanoparticle in precipitation synthesis method with 0.04 M Na_2SO_4 and 0.04 M $BaCl_2$.[271] The results show that the optimal concentration ratio for this method is 1 : 1 and increment of feed concentration would produce more homogenous and well-dispersed particles. Furthermore, the addition of 5 mL of the auxiliary solution as steric and electrostatic stabilizer results in better uniformity and significantly reduce particle size.[272–274] They hypothesized that the nanoparticle stabilization involves glycerol hydrophilic matter and liposome localization near the sulfate anions to change the chains configuration and subsequently prevent agglomeration.[275] Moreover, lower operation temperature at 0 °C is more suitable to minimize the growth of nanoparticles. $BaSO_4$ nanoparticles obtained from the optimal state at mixing rate of 900 rpm have an mean particle size of 12 nm.

Manteghian & Sameni (2019) synthesized $BaSO_4$ nanoparticles using starch and polyanionic cellulose (PAC) as stabilizer.[276] Starch is a polysaccharide composed of D-glucose residues with α-(1→4) linkages in linear amylose and approximately 5% α-(1→6) branch linkages in amylopectin, which are intertwined in starch granules that can expand and leach in heated water.[277,278] Polyanionic cellulose (PAC) is a derivative product of cellulose compound which is more superior over carboxymethyl cellulose (CMC) in terms of filtration reduction, anti-salt, anti-collapse and thermal stability.[279] PAC is mainly used as a renewable viscosifier additive in oil drilling.[280] PAC and starch stabilize $BaSO_4$ nanoparticles by carboxyl and hydroxyl groups formation in polymeric chains. Synthesis of $BaSO_4$ nanoparticles with 300 mg/25 cc starch by adding 21.3 mg/25 cc BaS and 135 mg/25 cc Na_2SO_4 as reactant would result in wider range of particle size between 33–140 nm and mean particle size of 58.7 nm, as shown in Fig. 16n, whereas SEM image in Fig. 16o reveals that $BaSO_4$ nanoparticles obtained with PAC at the same condition have particle sizes ranging from 10–58 nm with mean particle size of 18 nm. Due to longer chemical structure chains than starch, PAC would induce greater steric effect, hence have thicker protective layer surrounding $BaSO_4$ nanoparticles that more effectively passivating their surface to prevent any contact with the covered particle.[281,282]

6. Conclusions and future outlooks

Barium sulfate has gained interests due to its unique characteristics. This argument is proven by increasing barium sulfate production per year to ensure abundant supply in the industrial market, mainly for petroleum and polymer industry. Barium sulfate nanoparticles were developed to increase its market value while expanding the range of sectors that can be optimized with barium sulfate. Barium sulfate nanoparticles have been used in medical imaging technology and as polymer additives to increase its thermal stability. With its economically beneficial advantages in mind, bottom-up production of barium sulfate nanoparticles by direct precipitation method is the most widely developed synthesis route to this date. However, direct precipitation of barium sulfate by only using two main reactants as precursor without any additives and pH tuning often leads to higher agglomeration rate. To solve this issue, capping agent are added during precipitation to control the nucleation rate and growth of nanoparticles. These conditions directly causes the shift in optimal pH conditions and necessary amount of all reactants and additives in reaction. Based on the comparison of several capping agents used to produce $BaSO_4$ nanoparticles by precipitation method, surfactants such as DTAB, CTAB, ODP, and DBSA tend to produce larger particle sizes (56 nm to 289 nm) compared to polymers, which produce smaller particles ranging from 14 nm to 30 nm. This observation suggests that polymers might provide better control over nucleation and growth during particle synthesis, whereas the organic compound solvents have larger particle sizes, ranging from 16 nm to 208 nm, due to the different physical and chemical properties of each compound, including dynamic viscosity, polarity, and functional groups, which affect the interaction between the two phases in the chemical reaction. Nonetheless, this method still have some issues, such as the utilization of hazardous and toxic precipitating and capping agent. Ionic liquid proposed as an alternative capping agent that reduce the toxic waste material from barium sulfate nanoparticle precipitation. The selection of ionic liquid as capping agent for the precipitation of $BaSO_4$ nanoparticles must

consider several factors, including the hydrophobic and hydrophilic nature of ionic liquid, its molar conductivity, and its diffusivity in water. Another approach to developed green synthesis is proposed by using natural resources for conventional capping agent substitute. Some natural compounds, such as neem leaf extract, starch, polyanionic cellulose, and glycerol, have been reported to enhance the performance of $BaSO_4$ nanoparticle precipitation, resulting in a mean particle size ranging from 10 nm to 72 nm, relatively similar to that of $BaSO_4$ nanoparticles obtained from precipitation with other compounds. These natural compounds should be examined further to evaluate its reproducibility and stability in $BaSO_4$ precipitation reaction.

Furthermore, barium sulfate nanoparticles direct precipitation scale-up is explored by designing various types of reactors with their own capacity and characteristics. In a Rotating Packed Bed (RPB) reactor, the $BaSO_4$ nanoparticles precipitation reaction conducted at a rotating speed three times higher and involving organic solvents would dramatically decrease the obtained $BaSO_4$ particle size from 45 nm to 10 nm. Meanwhile, $BaSO_4$ nanoparticles precipitation in a T-mixer typically produces nanoparticles with a mean particle size around 70–80 nm, unless modified by using a capillary microreactor or adjusting the inlet tube angle to resemble a Y-mixer. These modifications increase the contact frequency and surface area, resulting in $BaSO_4$ nanoparticles with a smaller mean particle size of around 33–53 nm. Another type of reactor, namely spinning disc reactor (SDR), tends to highly depend on its high rotating speed and small disc diameter to produce fine $BaSO_4$ nanoparticles. On the same note, a membrane reactor produces fine particles ranging from 15 nm to 70 nm but requires more reaction time, as it works within a specific range of transmembrane pressure and has limited selectivity. Hence, reactor design, dimensions, flow rate, and rotating speed should be carefully considered before scaling-up this reaction process for specific industrial purposes.

Based on the comparisons data presented in this review, we conclude that further development of barium sulfate nanoparticles will more likely to continue the use of precipitation method in the liquid phase. With the external demand to find environmentally friendly synthesis routes, the most potential capping agents for further research are those based on organic compounds given their high availability and great dispersibility. The design of scale-up reactors that have prominent shear forces feature such as spinning disk reactors can be optimized to break up aggregates while maintaining the nucleation rate. Meanwhile, the performance of T-mixer and Y-mixer reactors as one of the most common reactor types can be improved by investigating the effect of solution flow rate and the length of pipelines on the rheology of the system which is related to the agglomeration rate and particle size distribution. Analysis of the effect of pressure variation on the nucleation rate in a closed reactor with a certain temperature can also be conducted to obtain a smaller final product with a narrower size distribution. Baffles may be used in a barium sulfate precipitation reactor to prevent vortex formation, significantly increasing the probability of achieving a more uniform distribution of reactants and resulting in a final product with an improved particle size distribution.

Barium sulfate nanoparticles have great prospects in the medical and polymer industries. Their surface-modifying capability can enhance both the base material's mechanical strength and its beneficial features to improve the base material's functionality, such as reduced water absorbance, a higher threshold for thermal decomposition, UV absorption, and serving as a tool to increase its economic worth. In conclusion, barium sulfate nanoparticles have significant potential in various biomedical and industrial applications due to their unique properties and functional versatility. Future research should focus on optimizing their synthesis and exploring innovative applications to fully harness their utilization in various sectors.

Data availability

No primary research results, software or code have been included and no new data were generated or analysed as part of this review.

Conflicts of interest

There are no conflicts to declare.

References

1 M. Nasrollahzadeh, S. M. Sajadi, M. Sajjadi and Z. Issaabadi, *Interface Sci. Technol.*, 2019, **28**, 1–27.
2 K. Ariga, Q. Ji, W. Nakanishi, J. P. Hill and M. Aono, *Mater. Horiz.*, 2015, **2**, 406–413.
3 J. Baxter, Z. Bian, G. Chen, D. Danielson, M. S. Dresselhaus, A. G. Fedorov and Y. Wu, *Energy Environ. Sci.*, 2009, **2**, 559–588.
4 A. C. Balazs, T. Emrick and T. P. Russell, *Science*, 2006, **314**, 1107–1110.
5 S. C. Thomas, P. Kumar Mishra and S. Talegaonkar, *Curr. Pharm. Des.*, 2015, **21**, 6165–6188.
6 V. V. Mody, R. Siwale, A. Singh and H. R. Mody, *J. Pharm. BioAllied Sci.*, 2010, **2**, 282–289.
7 D. Guo, G. Xie and J. Luo, *J. Phys. D: Appl. Phys.*, 2013, **47**, 013001.
8 I. Khan, K. Saeed and I. Khan, *Arabian J. Chem.*, 2019, **12**, 908–931.
9 M. W. McKee and R. W. Jurgens Jr, *Am. J. Hosp. Pharm.*, 1986, **43**, 145–148.
10 W. Wang, O. C. Zafiriou, I. Y. Chan, R. G. Zepp and N. V. Blough, *Environ. Sci. Technol.*, 2007, **41**, 1601–1607.
11 N. Knighton and B. Bugbee, *Tech. Instrum.*, 2005, **11**, 4–6.
12 E. G. Souza, K. Kruger, C. D. Nascimento, C. Aguzzoli, G. Hoff, A. C. B. Moraes and N. L. Carreno, *Polymers*, 2023, **15**, 4382.
13 K. Wang, J. Wu, L. Ye and H. Zeng, *Composites, Part A*, 2003, **34**, 1199–1205.
14 Y. Xiao, J. Yan, K. Hu, S. Pan, C. Du, X. Li and L. Li, in *Appl. Sci. Graph. Commun. Packag.: Proc. 2017 49th Conf. Int.*

Circle Educ. Inst. Graph. Arts Technol. Manag. & 8th China Acad. Conf. Print. Packag., Springer Singapore, 2018, pp. 753–759.
15 B. Li, X. Wang, Y. Ma, D. Pan, S. Maganti, B. Xu and Z. Guo, *ES Mater. Manuf.*, 2022, **17**, 83–91.
16 P. Mehnati, R. Malekzadeh and M. Y. Sooteh, *Nanomed. J.*, 2020, **7**, 170–182.
17 S. D. O'Connor and R. M. Summers, *Acad. Radiol.*, 2007, **14**, 72–80.
18 K. F. Qasim and M. A. Mousa, *Egypt. J. Pet.*, 2021, **30**, 9–19.
19 G. Trencsényi, C. Csikos and Z. Képes, *Int. J. Mol. Sci.*, 2024, **25**, 664.
20 T. Zhu, X. Zeng, J. Li, J. Liao, Z. Ma, X. Zuo and J. Nan, *J. Energy Storage*, 2024, **84**, 110841.
21 K. V. Jagannath and M. Kusuma, *Mater. Res. Express*, 2019, **6**, 095094.
22 J. Kozak and A. Townshend, in *Encycl. Anal. Sci.*, ed. P. Worsfold, C. Poole, A. Townshend and M. Miró, Academic Press, 3rd edn, 2019, pp. 111–120.
23 H. Wu, C. Wang, C. Zeng and L. Zhang, *Ind. Eng. Chem. Res.*, 2013, **52**, 5313–5320.
24 V. M. Arole and S. V. Munde, *J. Mater. Sci.*, 2014, **1**, 89–93.
25 H. Lu, S. Y. Tang, G. Yun, H. Li, Y. Zhang, R. Qiao and W. Li, *Biosensors*, 2020, **10**, 165.
26 P. Christian, F. Von der Kammer, M. Baalousha and T. Hofmann, *Ecotoxicology*, 2008, **17**, 326–343.
27 C. M. Patel, M. Chakraborty and Z. V. P. Murthy, *Adv. Powder Technol.*, 2014, **25**, 226–235.
28 N. G. Semaltianos, *Crit. Rev. Solid State Mater. Sci.*, 2010, **35**, 105–124.
29 B. A. Al Jahdaly, M. F. Elsadek, B. M. Ahmed, M. F. Farahat, M. M. Taher and A. M. Khalil, *Sustainability*, 2021, **13**, 2127.
30 D. Adityawarman, Precipitation of barium sulphate nanoparticles in microemulsion: Experiments and modelling, Doctoral dissertation, Otto-von-Guericke-Universität Magdeburg, 2007.
31 D. Adityawarman, A. Voigt, P. Veit and K. Sundmacher, *Chem. Eng. Sci.*, 2005, **60**, 3373–3381.
32 L. Zhang, W. Xie, S. Guo, X. Xia and S. Yang, *Chem. Eng. Process. Process Intensif.*, 2023, **184**, 109298.
33 Y. Chang, X. Yan, Q. Wang, L. Ren, J. Tong and J. Zhou, *Food Chem.*, 2017, **227**, 369–375.
34 D. Reay, C. Ramshaw and A. Harvey, *Process Intensification: Engineering for Efficiency, Sustainability and Flexibility*, Elsevier, 2008, p. 129.
35 G. A. Patil, M. L. Bari, B. A. Bhanvase, V. Ganvir, S. Mishra and S. H. Sonawane, *Chem. Eng. Process. Process Intensif.*, 2012, **62**, 69–77.
36 Q. A. Wang, J. X. Wang, M. Li, L. Shao, J. F. Chen, L. Gu and Y. T. An, *Chem. Eng. J.*, 2009, **149**, 473–478.
37 C. C. Li, S. J. Chang, F. J. Su, S. W. Lin and Y. C. Chou, *Colloids Surf., A*, 2013, **419**, 209–215.
38 M. Jha, S. Ansari and N. G. Shimpi, *Bull. Mater. Sci.*, 2019, **42**, 1–9.
39 L. Qi, H. Cölfen and M. Antonietti, *Chem. Mater.*, 2000, **12**, 2392–2403.
40 L. Qi, H. Cölfen, M. Antonietti, M. Li, J. D. Hopwood, A. J. Ashley and S. Mann, *Chem.–Eur. J.*, 2001, **7**, 3526–3532.
41 M. J. Meagher, B. Leone, T. L. Turnbull, R. D. Ross, Z. Zhang and R. K. Roeder, *J. Nanopart. Res.*, 2013, **15**, 1–10.
42 E. Akyol and M. A. Cedimagar, *Cryst. Res. Technol.*, 2016, **51**, 393–399.
43 J. Li, Y. Xu, D. Wu and Y. Sun, *China Particuol.*, 2003, **1**, 134–136.
44 S. Li, L. Zheng and L. Yu, *J. Dispersion Sci. Technol.*, 2011, **32**, 601–603.
45 I. C. Romero-Ibarra, G. Rodríguez-Gattorno, M. F. García-Sánchez, A. Sánchez-Solís and O. Manero, *Langmuir*, 2010, **26**, 6954–6959.
46 M. D. Najafi, S. K. Eshkalak, B. Amiri, H. R. Naderi, E. Kowsari, A. Chinnappan and S. Ramakrishna, *Mater. Today Chem.*, 2022, **23**, 100633.
47 A. M. Dehkordi and A. Vafaeimanesh, *Ind. Eng. Chem. Res.*, 2009, **48**, 7574–7580.
48 L. Fang, Q. Sun, Y. H. Duan, J. Zhai, D. Wang and J. X. Wang, *Front. Chem. Sci. Eng.*, 2021, **15**, 902–912.
49 H. B. Farahani, M. Shahrokhi and A. M. Dehkordi, *Chem. Eng. Process. Process Intensif.*, 2017, **115**, 11–22.
50 R. J. J. Jachuck and C. Ramshaw, *Heat Recovery Syst. CHP*, 1994, **14**, 475–491.
51 J. Zhiqian and L. Zhongzhou, *J. Membr. Sci.*, 2002, **209**, 153–161.
52 E. S. Borovinskaya and V. P. Reshetilovskii, *Russ. J. Appl. Chem.*, 2011, **84**, 1094–1104.
53 C. G. Barreras-Urbina, B. Ramírez-Wong, G. A. López-Ahumada, S. E. Burruel-Ibarra, O. Martínez-Cruz, J. A. Tapia-Hernández and F. Rodriguez Felix, *Int. J. Food Prop.*, 2016, **19**, 1912–1923.
54 S. Patil and S. Jagadale, in *Solution Methods for Metal Oxide Nanostructures*, Elsevier, 2023, pp. 39–60.
55 D. Moinard-Checot, Y. Chevalier, S. Briançon, H. Fessi and S. Guinebretière, *J. Nanosci. Nanotechnol.*, 2006, **6**, 2664–2681.
56 Y. Zare, *Composites, Part A*, 2016, **84**, 158–164.
57 Z. Yang and Z. Xia, in *Adv. Ceram. Energy Storage, Thermoelectr. Photonics*, ed. P. Cao, Z.-G. Chen and Z. Xia, Elsevier, 2023, pp. 395–429.
58 C. V. Restrepo and C. C. Villa, *Environ. Nanotechnol. Monit. Manag.*, 2021, **15**, 100428.
59 H. Bala, W. Fu, J. Zhao, X. Ding, Y. Jiang, K. Yu and Z. Wang, *Colloids Surf., A*, 2005, **252**, 129–134.
60 W. S. Ahn, G. J. Kim and G. Seo, in *Nanoporous Materials: Science and Engineering*, 2004, pp. 649–693.
61 J. Vaynberg and L. M. Ng, *Surf. Sci.*, 2005, **577**, 175–187.
62 V. Ramaswamy, R. M. Vimalathithan and V. Ponnusamy, *J. Ceram. Process. Res.*, 2011, **12**, 173–175.
63 V. Ramaswamy, R. M. Vimalathithan and V. Ponnusamy, *Adv. Mater. Lett.*, 2012, **3**, 29–33.
64 A. D. Jew, Q. Li, D. Cercone, K. Maher, G. E. Brown Jr and J. R. Bargar, *Proc. 6th Unconv. Resour. Technol. Conf.*, 2018, DOI: **10.15530/urtec-2018-2899671**.

65 L. I. Boguslavskii, T. M. Buslaeva, V. V. Fomichev, E. V. Kopylova, A. P. Kaplun and V. I. Popenko, *Russ. J. Phys. Chem. A*, 2015, **89**, 256–260.
66 J. E. Wesfreid, *C. R. Mec.*, 2017, **345**, 446–466.
67 R. J. P. Williams and J. J. R. Fraústo da Silva, in *The Chemistry of Evolution*, Elsevier Sci. Ltd, 2006, pp. 77–124.
68 W. Fyen, F. Holsteyns, T. Bearda, S. Arnauts, J. Van Steenbergen, G. Doumen, K. Kenis and P. W. Mertens, in *Dev. Surf. Contam. Clean.*, ed. R. Kohli and K. L. Mittal, William Andrew Publ., 2nd edn, 2008, pp. 795–854.
69 M. J. Nine, T. T. Tung and D. Losic, in *Compr. Supramol. Chem. II*, ed. J. L. Atwood, Elsevier, 2017, pp. 47–74.
70 Q.-J. Yang, Q. Mao and W. Cao, *Colloids Surf., A*, 2022, **639**, 128385.
71 Y. Shen, C. Li, X. Zhu, A. Xie, L. Qiu and J. Zhu, *J. Chem. Sci.*, 2007, **119**, 319–324.
72 M. Kucher, D. Babic and M. Kind, *Chem. Eng. Process. Process Intensif.*, 2006, **45**, 900–907.
73 F. Jones, J. Clegg, A. Oliveira, A. L. Rohl, M. I. Ogden, G. M. Parkinson and M. M. Reyhani, *CrystEngComm*, 2001, **3**, 165–167.
74 F. Jones, A. Oliveira, A. L. Rohl, M. I. Ogden and G. M. Parkinson, *CrystEngComm*, 2006, **8**, 869–876.
75 S. Auer and D. Frenkel, *Nature*, 2001, **413**, 711–713.
76 H. B. Singh and K. A. Bharati, in *Handbook of Natural Dyes and Pigments*, Woodhead Publishing, India, 2014, pp. 33–260.
77 Z. Mohammadi, S. Shalavi and H. Jafarzadeh, *Eur. J. Dent.*, 2013, **7**, S135–S142.
78 P. Ales and J. M. Davidson, in *Principles of Tissue Engineering*, ed. R. Lanza, R. Langer and J. Vacanti, Academic Press, 3rd edn, 2007, pp. 493–515.
79 W. Terakosolphan, J. L. Trick, P. G. Royall, S. E. Rogers, O. Lamberti, C. D. Lorenz, B. Forbes and R. D. Harvey, *Langmuir*, 2018, **34**, 6941–6954.
80 U. Paik, S. Lee and V. A. Hackley, *J. Am. Ceram. Soc.*, 2003, **86**, 1662–1668.
81 Q. Chen, H. Bao and X. Shen, *Radiat. Phys. Chem.*, 2008, **77**, 974–977.
82 L. Qian and X. Yang, *Electrochem. Commun.*, 2007, **9**, 393–397.
83 Y. Zhao and J. Liu, *Chem. Lett.*, 2006, **35**, 1040–1041.
84 E. Norkus, A. Vaškelis and I. Zakaitė, *Talanta*, 1996, **43**, 465–470.
85 Z. Ezzeddine, I. Batonneau-Gener, Y. Pouilloux, H. Hamad, Z. Saad and V. Kazpard, *Microporous Mesoporous Mater.*, 2015, **212**, 125–136.
86 H. S. Zhu, X. J. Yang, Y. P. Mao, Y. Chen, X. L. Long and W. K. Yuan, *J. Hazard. Mater.*, 2011, **185**, 951–957.
87 H. Xu, H. Tian, J. Deng, Q. Zhuo, J. Cui, J. Wang and P. Yu, *Miner. Eng.*, 2023, **203**, 108304.
88 L. Qi, H. Cölfen and M. Antonietti, *Angew. Chem., Int. Ed.*, 2000, **39**, 604–607.
89 M. C. Van dor Leeden and G. M. Van Rosmalen, *SPE Prod. Eng.*, 1990, **5**, 70–76.
90 C. She, J. Guo, S. Irle, K. Morokuma, D. L. Mohler, H. Zabri and T. Lian, *J. Phys. Chem. A*, 2007, **111**, 6832–6842.
91 G. A. Mun, V. V. Khutoryanskiy, G. T. Akhmetkalieva, S. N. Shmakov, A. V. Dubolazov, Z. S. Nurkeeva and K. Park, *Colloid Polym. Sci.*, 2004, **283**, 174–181.
92 Y. L. Luo, W. Yu and F. Xu, *Polym. Bull.*, 2012, **69**, 597–620.
93 F. Wang, G. Xu, Z. Zhang and X. Xin, *Colloids Surf., A*, 2005, **259**, 151–154.
94 H. Cölfen and S.-H. Yu, *MRS Bull.*, 2005, **30**, 727–735.
95 A. Parmar, B. Bharatiya, K. Patel, V. Aswal and P. Bahadur, *J. Surfactants Deterg.*, 2012, **16**, 105–114.
96 Y. Hartanto, Y. Yaswari, M. Zunita, T. H. Soerawidjaja and A. Indarto, *Sep. Sci. Technol.*, 2017, **52**, 1967–1972.
97 V. Singh, P. Khullar, P. N. Dave and N. Kaur, *Int. J. Ind. Chem.*, 2013, **4**, 12.
98 M. E. Saraya and I. M. Bakr, *Am. J. Nanotechnol.*, 2011, **2**, 106–111.
99 P. K. S. Mural, G. Madras and S. Bose, *Nano-Struct. Nano-Objects*, 2018, **14**, 149–165.
100 A. Jose, T. Mathew, N. Fernández-Navas and C. J. Querebillo, *Micro*, 2024, **4**, 229–280.
101 N. Nandakumar and P. Kurian, *Powder Technol.*, 2012, **224**, 51–56.
102 I. P. Indrayana, L. A. Tjuana, M. T. Tuny and K. Kurnia, *J. Phys.: Conf. Ser.*, 2019, **1341**, 012045.
103 S. Bagheri, K. G. Chandrappa and S. B. A. Hamid, *Pharma Chem.*, 2013, **5**, 265–270.
104 Y. Sun, F. Zhang, D. Wu and H. Zhu, *Particuology*, 2014, **14**, 33–37.
105 A. W. M. De Laat, *Adsorption of Water-Soluble Polymers onto Barium Titanate and its Effects on Colloidal Stability*, Wageningen University and Research, 1995.
106 G. H. Kirby, D. J. Harris, Q. Li and J. A. Lewis, *J. Am. Ceram. Soc.*, 2004, **87**, 181–186.
107 A. Gupta, P. Singh and C. Shivakumara, *Solid State Commun.*, 2010, **150**, 386–388.
108 D. N. Unal, S. Sadak, C. Erkmen, Ö. Selcuk and B. Uslu, in *Surfactant-Based Sensors in Chemical and Biochemical Detection*, ed. J. G. Manjunatha, Royal Society of Chemistry, 2023, ch. 1, vol. 23, pp. 1–18.
109 A. Durán-Álvarez, M. Maldonado-Domínguez, O. González-Antonio, C. Durán-Valencia, M. Romero-Ávila, F. Barragán-Aroche and S. López-Ramírez, *Langmuir*, 2016, **32**, 2608–2616.
110 C. Zhao, F. Liu, W. Kang, Y. Su, D. Wang and Q. Shen, *Cryst. Growth Des.*, 2011, **11**, 2084–2090.
111 H. Bala, W. Fu, Y. Guo, J. Zhao, Y. Jiang, X. Ding, K. Yu, M. Li and Z. Wang, *Colloids Surf., A*, 2006, **274**, 71–76.
112 Y. Li, X. Wang, Y. Cui, W. Ma and H. Guo, *Int. J. Nanosci.*, 2012, **11**, 1240040.
113 K. E. Johnson, *Electrochem. Soc. Interface*, 2007, **16**, 38.
114 M. Zunita, A. Raizki, R. Aditya and I. G. Wenten, *Results Eng.*, 2022, **16**, 100653.
115 I. G. B. N. Makertihartha, M. Zunita, P. T. Dharmawijaya and I. G. Wenten, *AIP Conf. Proc.*, 2017, **1788**, 020019.
116 M. Zunita, D. Wahyuningrum, B. Buchari, B. Bundjali and I. G. Wenten, *Org. Prep. Proced. Int.*, 2021, **53**, 151–156.
117 N. Keppeler, P. D. Galgano, M. Schönhoff, N. I. Malek and O. A. El Seoud, *J. Mol. Liq.*, 2022, **362**, 119681.

118 C. S. Buettner, A. Cognigni, C. Schröder and K. Bica-Schröder, *J. Mol. Liq.*, 2022, **347**, 118160.
119 J. A. Siddique, A. Ahmad and M. Jawaid, in *Advances in Green and Sustainable Chemistry: Ionic Liquids and Their Application in Green Chemistry*, Elsevier, 2023, pp. xxvii–xxviii.
120 M. Zunita and R. D. Rhamadhani, *ASEAN J. Chem. Eng.*, 2021, **21**, 249–271.
121 V. A. Rahmi and M. Zunita, *AIP Conf. Proc.*, 2024, **3073**, 030003.
122 T. Welton, *Green Chem.*, 2011, **13**, 225.
123 M. Zunita and V. A. Rahmi, *Chem. Afr.*, 2024, **7**, 505–538.
124 M. Zunita, H. P. Winoto, M. F. K. Fauzan and R. Haikal, *Polym. Degrad. Stab.*, 2023, **211**, 110320.
125 M. Kowacz, P. Groves, J. M. Esperanca and L. P. N. Rebelo, *Cryst. Growth Des.*, 2011, **11**, 684–691.
126 K. Dill and S. Bromberg, *Molecular Driving Forces: Statistical Thermodynamics in Biology, Chemistry, Physics, and Nanoscience*, Garland Science, 2003, p. 327.
127 P. Tsai and E. Lee, *Soft Matter*, 2011, **7**, 5789.
128 D. Banerjee, S. S. Sinha and S. K. Pal, *J. Phys. Chem. B*, 2007, **111**, 14239–14243.
129 M. G. Freire, L. M. Santos, A. M. Fernandes, J. A. Coutinho and I. M. Marrucho, *Fluid Phase Equilib.*, 2007, **261**, 449–454.
130 M. Zunita, W. Natola, M. David and G. Lugito, *Chem. Eng. J. Adv.*, 2022, **11**, 100320.
131 M. Zunita, D. Wahyuningrum, B. Buchari, B. Bundjali, I. G. Wenten and R. Boopathy, *Appl. Sci.*, 2021, **11**, 989.
132 C. Spickermann, J. Thar, S. B. C. Lehmann, S. Zahn, J. Hunger, R. Buchner and B. Kirchner, *J. Chem. Phys.*, 2008, **129**, 104505.
133 I. Chorny and I. Benjamin, *J. Phys. Chem. B*, 2005, **109**, 16455–16462.
134 M. N. Rodnikova, *Russ. J. Electrochem.*, 2003, **39**, 192–197.
135 M. Zunita, D. Wahyuningrum and B. Bundjali, *Int. J. Electrochem. Sci.*, 2012, **7**, 3274–3288.
136 M. Videa, W. Xu, B. Geil, R. Marzke and C. A. Angell, *J. Electrochem. Soc.*, 2001, **148**, A1352.
137 C. A. Cassou and E. R. Williams, *Analyst*, 2014, **139**, 4810–4819.
138 D. R. MacFarlane, M. Kar and J. M. Pringle, *Fundamentals of Ionic Liquids: From Chemistry to Applications*, Wiley, 2017.
139 Y. Marcus, *Ionic Liquid Properties: From Molten Salts to RTILs*, Springer, 2016.
140 S. Zhang, X. Lu, Q. Zhou, X. Li, X. Zhang and S. Li, in *Ionic Liquids*, 2009, pp. 23–197.
141 A. Kaur, S. Bansal, D. Chauhan, K. K. Bhasin and G. R. Chaudhary, *J. Mol. Liq.*, 2019, **286**, 110878.
142 D. Połomski, P. Garbacz, K. Czerwinski and M. Chotkowski, *J. Mol. Liq.*, 2021, **327**, 114820.
143 H. Zhang, M. L. Ferrer, M. J. Roldan-Ruiz, R. J. Jiménez Rioboó, M. C. Gutierrez and F. del Monte, *J. Phys. Chem. B*, 2020, **124**, 943–951.
144 F. S. S. Oliveira, PhD thesis, Universidade NOVA de Lisboa, 2015.
145 C. M. Ng, P. C. Chen and S. Manickam, *Ind. Eng. Chem. Res.*, 2012, **51**, 5375–5381.
146 K. Neumann, K. Gladyszewski, K. Groß, H. Qammar, D. Wenzel, A. Górak and M. Skiborowski, *Chem. Eng. Res. Des.*, 2018, **134**, 443–462.
147 J. F. Chen, Y. H. Wang, F. Guo, X. M. Wang and C. Zheng, *Ind. Eng. Chem. Res.*, 2000, **39**, 948–954.
148 Y. H. Chen, C. Y. Chang, W. L. Su, C. C. Chen, C. Y. Chiu, Y. H. Yu and S. I. Chiang, *Ind. Eng. Chem. Res.*, 2004, **43**, 228–236.
149 D. P. Rao, A. Bhowal and P. S. Goswami, *Ind. Eng. Chem. Res.*, 2004, **43**, 1150–1162.
150 L. Sang, Y. Luo, G. W. Chu, Y. Z. Liu, X. Z. Liu and J. F. Chen, *Chem. Eng. Sci.*, 2017, **170**, 355–364.
151 C. L. Duan, X. Liu, B. Shan and R. Chen, *Rev. Sci. Instrum.*, 2015, **86**, 075110.
152 X. Yang, G. Chu, L. Wen, K. Yang, G. Xiao and J. Chen, *Particuology*, 2010, **8**, 372–378.
153 H. Li and D. Xu, *Theor. Appl. Mech. Lett.*, 2023, 100466.
154 A. Husain, A. I. Khan, W. Raza, N. Al-Rawahi, N. Al-Azri and A. Samad, *J. Eng. Res.*, 2022, **19**, 106–128.
155 D. Bothe, C. Stemich and H. J. Warnecke, *Chem. Eng. Sci.*, 2006, **61**, 2950–2958.
156 Z. Dong, Z. Wen, F. Zhao, S. Kuhn and T. Noël, *Chem. Eng. Sci.:X*, 2021, **10**, 100097.
157 H. C. Schwarzer and W. Peukert, *Chem. Eng. Technol.*, 2002, **25**, 657–661.
158 D. A. Barlow, J. K. Baird and C. H. Su, *J. Cryst. Growth*, 2004, **264**, 417–423.
159 J. Gradl and W. Peukert, in *Micro and Macro Mixing: Analysis, Simulation and Numerical Calculation*, Springer Berlin Heidelberg, Berlin, Heidelberg, 2010, pp. 105–124.
160 L. Lindfors, S. Forssén, J. Westergren and U. Olsson, *J. Colloid Interface Sci.*, 2008, **325**, 404–413.
161 L. Li, A. J. Fijneman, J. A. Kaandorp, J. Aizenberg and W. L. Noorduin, *Proc. Natl. Acad. Sci. U. S. A.*, 2018, **115**, 3575–3580.
162 M. Pieper, S. Aman, W. Hintz and J. Tomas, *Chem. Eng. Technol.*, 2011, **34**, 1567–1574.
163 S. Nakade, M. Matsuda, S. Kambe, Y. Saito, T. Kitamura, T. Sakata, Y. Wada, H. Mori and S. Yanagida, *J. Phys. Chem. B*, 2002, **106**, 10004–10010.
164 N. Kockmann, *Proc. Inst. Mech. Eng., Part C*, 2008, **222**, 807–816.
165 V. S. T. Madana and B. Ashraf Ali, *Phys. Fluids*, 2020, **32**, 072003.
166 N. T. Nguyen and Z. Wu, *J. Micromech. Microeng.*, 2004, **15**, R1–R16.
167 B. Bhanvase and D. Barai, in *Nanofluids for Heat and Mass Transfer*, Academic Press, 2021, ch. 4, pp. 69–97.
168 H. Wang, A. Mustaffar, A. N. Phan, V. Zivkovic, D. Reay, R. Law and K. Boodhoo, *Chem. Eng. Process.*, 2017, **118**, 78–107.
169 M. Jiao, J. Zeng, L. Jing, C. Liu and M. Gao, *Chem. Mater.*, 2015, **27**, 1299–1305.

170 M. Outokesh, M. Hosseinpour, S. J. Ahmadi, T. Mousavand, S. Sadjadi and W. Soltanian, *Ind. Eng. Chem. Res.*, 2011, **50**, 3540–3554.
171 K. Oualha, M. Ben Amar and A. Kanaev, in *Computational Methods and Experimental Testing in Mechanical Engineering*, Springer, Cham, 2019, pp. 1–8.
172 J. van der Schaaf and J. C. Schouten, *Curr. Opin. Chem. Eng.*, 2011, **1**, 84–88.
173 L. M. Cafiero, G. Baffi, A. Chianese and R. J. J. Jachuck, *Ind. Eng. Chem. Res.*, 2002, **41**, 5240–5246.
174 K. Boodhoo, in *Process Intensification for Green Chemistry: Engineering Solutions for Sustainable Chemical Processing*, ed. K. Boodhoo and A. Harvey, Wiley-VCH, 2013, pp. 59–90.
175 M. Doble and A. K. Kruthiventi, in *Green Chemistry and Engineering*, Academic Press, 2007, ch. 4, pp. 105–170.
176 B. de Caprariis, M. Di Rita, M. Stoller, N. Verdone and A. Chianese, *Chem. Eng. Sci.*, 2012, **76**, 73–80.
177 R. Mohanty, S. Bhandarkar, B. Zuromski, R. Brown and J. Estrin, *AIChE J.*, 1988, **34**, 2063–2068.
178 J. Jahanshahi-Anboohi and A. Molaei Dehkordi, *Ind. Eng. Chem. Res.*, 2019, **58**, 16597–16609.
179 R. Kancherla, S. Nazia, S. Kalyani and S. Sridhar, *Comput. Chem. Eng.*, 2021, **148**, 107258.
180 C. Charcosset, S. Bernard, K. Fiaty, M. Bechelany and D. Cornu, *Curr. Opin. Chem. Eng.*, 2007, **1**, 15–23.
181 T. Sehayek, M. Lahav, R. Popovitz-Biro, A. Vaskevich and I. Rubinstein, *Chem. Mater.*, 2005, **17**, 3743–3748.
182 K. K. Sirkar, P. V. Shanbhag and A. S. Kovvali, *Ind. Eng. Chem. Res.*, 1999, **38**, 3715–3737.
183 L. Giorno, E. Drioli and H. Strathmann, in *Encyclopedia of Membranes*, Springer, Berlin, Heidelberg, 2016, pp. 1–6.
184 J. Pellegrino, L. R. Schulte, J. De la Cruz and C. Stoldt, *J. Membr. Sci.*, 2017, **522**, 245–256.
185 Z. Jia, Z. Liu and F. He, *J. Colloid Interface Sci.*, 2003, **266**, 322–327.
186 G. G. Chen, G. S. Luo, J. H. Xu and J. D. Wang, *Powder Technol.*, 2004, **139**, 180–185.
187 L. Du, Y. J. Wang, Y. C. Lu and G. S. Luo, *Powder Technol.*, 2013, **247**, 60–68.
188 D. M. Zarkadas and K. K. Sirkar, *Chem. Eng. Sci.*, 2006, **61**, 5030–5048.
189 R. Kieffer, C. Charcosset, F. Puel and D. Mangin, *Comput. Chem. Eng.*, 2008, **32**, 1325–1333.
190 R. Kieffer, D. Mangin, F. Puel and C. Charcosset, *Chem. Eng. Sci.*, 2009, **64**, 1759–1767.
191 K. Loza, I. Föhring, J. Bünger, G. A. Westphal, M. Köller, M. Epple and C. Sengstock, *Nanotoxicology*, 2016, **10**, 1492–1502.
192 K. R. Sneha and G. S. Sailaja, *J. Mater. Chem. B*, 2021, **9**, 8569–8593.
193 H. A. Maghrabi, A. Vijayan, F. Mohaddes, P. Deb and L. Wang, *Fibers Polym.*, 2016, **17**, 2047–2054.
194 E. Larsson, Evaluation of the Dual-Modal usage of contrast agents by means of Synchrotron X-ray Computed Microtomography and Magnetic Resonance Imaging using Macrophages loaded with Barium Sulfate and Gadolinium Nanoparticles for Detection and Monitoring in Animal Disease Models, PhD dissertation, Linköping University Electronic Press, Linköping, 2015.
195 M. Lopresti, L. Palin, G. Alberto, S. Cantamessa and M. Milanesio, *Mater. Today Commun.*, 2021, **26**, 101888.
196 T. Abdolahzadeh, J. Morshedian and S. Ahmadi, *Int. J. Radiat. Res.*, 2023, **21**, 79–87.
197 H. I. Kilian, H. Zhang, M. M. Shiraz Bhurwani, A. M. Nilam, D. Seong, M. Jeon, C. N. Ionita, J. Xia and J. F. Lovell, *J. Biomed. Opt.*, 2023, **28**, 082803.
198 D. A. O. Modena, A. C. G. Miranda, C. Grecco, R. E. Liebano, R. C. T. Cordeiro and R. M. Guidi, *Laser Med. Sci.*, 2020, **35**, 797–806.
199 R. Tokonami, M. Osanai, M. Hosoda, S. Tokonami and T. Takahashi, *Polym. Compos.*, 2024, **45**, 7519–7529.
200 R. Andrews, D. Jacques, D. Qian and T. Rantell, *Acc. Chem. Res.*, 2002, **35**, 1008–1017.
201 A. Bhatt, A. Jain, E. Gurnany, R. Jain, A. Modi and A. Jain, in *Nanoarchitectonics for Smart Delivery and Drug Targeting*, 2016, pp. 465–501.
202 P. H. Toy, in *Encyclopedia of Reagents for Organic Synthesis*, 2003.
203 G. Clave and S. Campidelli, *Chem. Sci.*, 2011, **2**, 1887–1896.
204 Z. Li, S. Guo, W. Song and Y. Yan, *J. Polym. Sci., Part B: Polym. Phys.*, 2002, **40**, 1804–1812.
205 H. Leng, X. Wang, G. L. Niebur and R. K. Roeder, *Ceram. Nanomater. Nanotechnol. III*, 2005, vol. 159, pp. 217–229.
206 S. M. Turley, A. Thambyah, C. M. Riggs, E. C. Firth and N. D. Broom, *J. Anat.*, 2014, **224**, 647–658.
207 Z. Seref-Ferlengez, O. D. Kennedy and M. B. Schaffler, *BoneKEy Rep.*, 2015, **4**, 708.
208 H. L. Frost, *Henry Ford Hosp. Med. J.*, 1960, **8**, 25–35.
209 H. Leng, X. Wang, R. D. Ross, G. L. Niebur and R. K. Roeder, *J. Mech. Behav. Biomed. Mater.*, 2008, **1**, 68–75.
210 F. M. Lambers, A. R. Bouman, C. M. Rimnac and C. J. Hernandez, *PLoS One*, 2013, **8**, e83662.
211 C. Fang, R. Hou, K. Zhou, F. Hua, Y. Cong, J. Zhang, J. Fu and Y. J. Cheng, *J. Mater. Chem. B*, 2014, **2**, 1264–1274.
212 P. Berning, M. Fekom, M. Ngoya, A. H. Goldstone, P. Dreger, S. Montoto, H. Finel, E. Shumilov, P. Chevallier, D. Blaise and T. Strüssmann, *Blood Cancer J.*, 2024, **14**, 106.
213 Y. Dang and J. Guan, *Smart Mater. Med.*, 2020, **1**, 10–19.
214 M. Kamal and P. Sethi, Case of Liver Metastasis for RFA, in *Problem Based Learning Discussions in Onco-Anesthesia and Onco-Critical Care*, Springer Nature Singapore, Singapore, 2024, pp. 249–253.
215 S. Walter, T. Weinschenk, A. Stenzl, R. Zdrojowy, A. Pluzanska, C. Szczylik, M. Staehler, W. Brugger, P.-Y. Dietrich, R. Mendrzyk, N. Hilf, O. Schoor, J. Fritsche, A. Mahr, D. Maurer, V. Vass, C. Trautwein, T. Lewandrowski, C. Flohr, H. Pohla, J. J. Stanczak, V. Bronte, S. Mandruzzato, T. Biedermann, G. Pawelec, E. Derhovanessian, H. Yamagishi, T. Miki, F. Hongo, N. Takaha, K. Hirakawa, H. Tanaka, S. Stevanovic, J. Frisch, A. Mayer-Mokler, A. Kirner, H.-G. Rammensee, C. Reinhardt and H. Singh-Jasuja, *Nat. Med.*, 2012, **18**, 1254–1261.

216 M. Makvandi, E. Dupis, J. W. Engle, F. M. Nortier, M. E. Fassbender, S. Simon, E. R. Birnbaum, R. W. Atcher, K. D. John, O. Rixe and J. P. Norenberg, *Targeted Oncol.*, 2018, **13**, 189–203.
217 S. Aghevlian, A. J. Boyle and R. M. Reilly, *Adv. Drug Deliv. Rev.*, 2017, **109**, 102–118.
218 F. Rösch, *Radiochim. Acta*, 2007, **95**, 303–311.
219 F. Reissig, R. Hübner, J. Steinbach, H. J. Pietzsch and C. Mamat, *Inorg. Chem. Front.*, 2019, **6**, 1341–1349.
220 A. Majkowska-Pilip, W. Gawęda, K. Żelechowska-Matysiak, K. Wawrowicz and A. Bilewicz, *Nanomaterials*, 2020, **10**, 1366.
221 F. Reissig, K. Zarschler, R. Hübner, H. J. Pietzsch, K. Kopka and C. Mamat, *ChemistryOpen*, 2020, **9**, 797–805.
222 F. Fiore, M. Del Prete, R. Franco, V. Marotta, F. Marciello, A. Di Sarno, A. C. Carratù, C. L. di Roseto, A. Colao and A. Faggiano, *Endocrine*, 2014, **47**, 177–182.
223 M. A. Londoño, A. D. Vallejo, L. F. A. Argueta, J. R. Uribe and A. R. Jaramillo, *Rev. Colomb. Cardiol.*, 2017, **28**, 4773–4781.
224 Y. X. J. Wáng, T. De Baere, J. M. Idée and S. Ballet, *Chin. J. Cancer Res.*, 2015, **27**, 96.
225 Q. Wang, K. Qian, S. Liu, Y. Yang, B. Liang, C. Zheng, X. Yang, H. Xu and A. Q. Shen, *Biomacromolecules*, 2015, **16**, 1240–1246.
226 A. Shukla and S. Kumar, *Development of Carrageenan-Linked Barium Sulphate Nanoparticles for Selective Tumor Cell Diagnosis and Treatment*, 2023.
227 M. Ahmadzadeh, M. Mirzaei, Z. Sabouri and M. Darroudi, *Inorg. Chem. Commun.*, 2024, **160**, 111904.
228 O. Manero and A. Sanchez-Solis, in *Handbook of Polymer Synthesis, Characterization, and Processing*, 2013, pp. 585–604.
229 X. Chen, L. Wang, J. Shi, H. Shi and Y. Liu, *Polym. Polym. Compos.*, 2009, **18**, 145–152.
230 M. Fisch and R. Bacaloglu, *J. Vinyl Addit. Technol.*, 1998, **4**, 4–11.
231 G. Zhao, L. Shi, D. Zhang, X. Feng, S. Yuan and J. Zhuo, *Mater. Des.*, 2012, **35**, 847–853.
232 A. S. Abyzov, L. N. Davydov and J. W. Schmelzer, *Entropy*, 2019, **21**, 782.
233 B. Wang, R. Utzeri, M. Castellano, P. Stagnaro, A. J. Müller and D. Cavallo, *Macromolecules*, 2020, **53**, 5980–5991.
234 E. Akdoğan, *Eur. J. Teach.*, 2020, **10**, 25–37.
235 Y. Li, D. Li, H. Cheng, C. Han and L. Xiao, *Polym. Test.*, 2023, **123**, 108050.
236 P. A. Ciullo and N. Hewitt, in *The Rubber Formulary*, William Andrew Publ., 1999, pp. 55–72.
237 Y. Li, X. Wang, X. Mu and S. Zhang, *Int. J. Nanosci.*, 2012, **11**, 1240039.
238 Y. Yang, C. Li, S. Yang, Q. Zhang and J. Xu, *J. Petrol. Sci. Eng.*, 2014, **124**, 19–26.
239 B. J. Anderson and C. F. Zukoski, *Langmuir*, 2010, **26**, 8709–8720.
240 M. S. de Carvalho, J. B. Azevedo and J. D. V. Barbosa, *Polym. Test.*, 2020, **90**, 106678.
241 I. C. Um, C. S. Ki, H. Kweon, K. G. Lee, D. W. Ihm and Y. H. Park, *Int. J. Biol. Macromol.*, 2004, **34**, 107–119.
242 W. Gao, B. Zhou, X. Ma, Y. Liu, Z. Wang and Y. Zhu, *Colloids Surf., A*, 2011, **385**, 181–187.
243 W. Gao, Z. Wang, Z. Zhao, L. Ding and Y. Zhu, *J. Therm. Anal. Calorim.*, 2017, **129**, 1047–1055.
244 R. D. Kulkarni, N. Ghosh, U. D. Patil and S. Mishra, *Polym. Compos.*, 2013, **34**, 1670–1681.
245 K. W. Ahmed and R. M. A. Hasan, *Zanco J. Med. Sci.*, 2017, **21**, 1818–1828.
246 I. C. Romero-Ibarra, E. Bonilla-Blancas, A. Sanchez-Solis and O. Manero, *Eur. Polym. J.*, 2012, **48**, 670–676.
247 H. Agarwal, S. Yadav and G. Jaiswar, *J. Therm. Anal. Calorim.*, 2017, **129**, 1471–1479.
248 A. J. de Jesus Silva, M. M. Contreras, C. R. Nascimento and M. F. da Costa, *Heliyon*, 2020, **6**, e04400.
249 S. He, S. Zhai, C. Zhang, Y. Xue, W. Yang and J. Lin, *Polymers*, 2019, **11**, 676.
250 M. N. Ahmad, S. Nadeem, S. Ul Hassan, S. Jamil, M. U. Javed, A. Mohyuddin, S. Haroon, T. Akhtar, A. Rauf and H. M. Raza, *Dig. J. Nanomater. Biostruct.*, 2021, 100–102.
251 T. Wu, Q. Zou, Z. Li, B. Chen, W. Gao, Q. Sun and S. Zhao, *Langmuir*, 2023, **40**, 638–646.
252 M. Huston, M. DeBella, M. DiBella and A. Gupta, *Nanomaterials*, 2021, **11**, 2130.
253 Á. B. Sifontes, E. Cañizales, J. Toro-Mendoza, E. Ávila, P. Hernández, B. A. Delgado, G. B. Gutiérrez, Y. Díaz and E. Cruz-Barrios, *J. Nanomater.*, 2015, **2015**, 510376.
254 L. Chen, J. Wang, H. Wang, Y. Zheng, Z. Qi, G. Chang, S. Xu, R. Li, T. Wu and W. Xu, in *MATEC Web Conf.*, EDP Sci., 2016, vol. 67, p. 02017.
255 A. Berman, J. Hanson, L. Leiserowitz, T. F. Koetzle, S. Weiner and L. Addadi, *Science*, 1993, **259**, 776–779.
256 R. L. Brutchey, E. S. Yoo and D. E. Morse, *J. Am. Chem. Soc.*, 2006, **128**, 10288–10294.
257 P. Calvert, *Scr. Metall. Mater.*, 1994, **31**, 977–982.
258 J. J. De Yoreo, *AIP Conf. Proc.*, 2010, **1270**, 45–58.
259 H. S. K. Al-Jadidi and M. A. Hossain, *Beni-Suef Univ. J. Basic Appl. Sci.*, 2015, **4**, 93–98.
260 R. Kumar, S. Mehta and S. R. Pathak, in *Synthesis of Medicinal Agents from Plants*, Elsevier, 2018, pp. 75–103.
261 I. S. Reddy and P. Neelima, *Int. J. Econ. Plants*, 2022, **9**, 59–63.
262 R. Sandhir, M. Khurana and N. K. Singhal, *Neurochem. Int.*, 2021, **146**, 105023.
263 Z. Sun, Z. Li, C. Huang, Y. Zhao, H. Zhang, R. Tao and Z. Liu, *Carbon*, 2011, **49**, 4376–4384.
264 Y. Tao and D. W. Sun, *Crit. Rev. Food Sci. Nutr.*, 2015, **55**, 570–594.
265 S. Saravanan, B. A. Kumar, S. B. Ronald and C. U. B. Rao, *J. Environ. Nanotechnol.*, 2024, **13**, 92–96.
266 P. Gupta and S. Phulara, in *Biotechnology of Terpenoid Production from Microbial Cell Factories*, Academic Press, 2021, pp. 133–156.
267 E. Su and D. Wei, *J. Mol. Catal. B: Enzym.*, 2008, **55**, 118–125.
268 P. Wang, in *Bioprocessing for Value-Added Products from Renewable Resources*, Elsevier, 2007, pp. 325–350.
269 P. Nalawade, T. Mukherjee and S. Kapoor, *Adv. Nanoparticles*, 2013, **2**, 78–86.

270 R. Parveen and G. Tremiliosi-Filho, *RSC Adv.*, 2016, **6**, 95210–95219.
271 S. Hosseini, K. Farhadi and S. Banisaeid, *J. Energy Storage*, 2019, **21**, 139–148.
272 F. Frusteri, F. Arena, G. Bonura, C. Cannilla, L. Spadaro and O. Di Blasi, *Appl. Catal., A*, 2009, **367**, 77–83.
273 Z. Khammar, E. Sadeghi, S. Raesi, R. Mohammadi, A. Dadvar and M. Rouhi, *Biocatal. Agric. Biotechnol.*, 2022, **43**, 102425.
274 V. Vagenende, M. G. Yap and B. L. Trout, *Biochemistry*, 2009, **48**, 11084–11096.
275 B. Tőkés, J. Száva, S. Duşa, L. Ferencz, A. Vintilă and G. Donáth-Nagy, *Pharmazie*, 2008, **63**, 185–193.
276 M. Manteghian and A. Sameni, *J. Nanostruct.*, 2019, **9**, 316–325.
277 L. M. Nwokocha and P. A. Williams, *Carbohydr. Polym.*, 2011, **84**, 395–401.
278 J. F. Robyt, in *Carbohydrate-active Enzymes: Structure, Function and Applications*, 2008, vol. 163, p. 3.
279 M. Li, S. Gu, J. Jin, Y. Zheng and D. Xie, *Constr. Build. Mater.*, 2020, **259**, 119841.
280 V. Mahto and V. P. Sharma, *J. Pet. Sci. Eng.*, 2004, **45**, 123–128.
281 L. Ortega-Arroyo, E. S. Martin-Martinez, M. A. Aguilar-Mendez, A. Cruz-Orea, I. Hernandez-Pérez and C. Glorieux, *Starch/Staerke*, 2013, **65**, 814–821.
282 N. S. Tapak, M. A. Nawawi, A. H. Mohamed, E. T. T. Tjih, Y. Mohd, A. H. B. Ab Rashid, J. Abdullah, N. A. Yusof and N. M. Ahmad, *Malays. J. Anal. Sci.*, 2022, **26**, 1394–1420.